# INTERACTION OF MICROWAVE RADIATION WITH AN INHOMOGENEOUS NONSTATIONARY PLASMA COLUMN*

*Božidar V. Stanić*

## 0. INTRODUCTION

In the well known monographs by L. M. BREHOVSKIH [2], V. L. GINZBURG [8] and H. C. VAN DER HULST [11] scattering problems concerning plane and spherical geometry have been treated extensively.

Scattering by cylindrical bodies has been, for the first time, theoretically treated by RAYLEIGH [50] and independently by W. VON IGNATOWSKI [35] for the case $R/\lambda \ll 1$, where $R$ is cylinder radius and $\lambda$ is free space wavelength of electromagnetic waves. Cases with $R/\lambda \gg 1$ have been treated by the geometrical optics approximation (D. J. WORT [57], M. A. HEALD [33] and others). J. SHMOYS [51] proposed some possible diagnostic technique for measuring electron density in plasma column by measuring scattering angle of microwave beam in function of impact parameter. KHARADLY [40] experimentally determined electron density distribution in plasma column measuring the distance between the places where microwave beam enter and emerge from plasma. ANIČIN [23] has measured scattering angle variation with impact parameter and obtained electron density profile. All these experiments used single frequency technique. L. A. DUSHIN [30] used many (three) frequencies technique for measuring electron density profiles in plasma column.

Y. MIDZUNO ([43] and [44]) has treated theoretically scattering by inhomogeneous underdense plasma column in free space using known, from the quantum mechanics, BORN approximation. In these cases for slow variation of electron density it is possible to use JBKW approximation also.

When the parameter $R/\lambda$ is near to one, and plasma is enclosed by the glass tube, the exact contour problem defined by MAXWELL equations must be solved. PLATZMAN and OZAKI [49] have treated theoretically the case of homogeneous plasma column and gave the expressions for scattering field and scattering cross section for both cases of polarization. KERKER and MATIJEVIĆ [41] gave the expressions for scattering field by inhomogeneous very thin fibres. They devided cylinder in many coaxial cylindrical sheets and considered each of them as homogeneous. LÜNOV and TUTER [42] devided cylindrical plasma column in ten sheets and for the electron density distribution of Gaussian form $n_e = n_{e0} \exp(-a^2 r^2)$ compared results of geometrical diffraction theory with the results of sheet theory. Independently, the similar approach has been done by

---

STANIĆ and WOODING [55] for different electron density profiles as

$$n_e = n_{e0}(1 - r^\gamma / R^\gamma), \quad \gamma = 0.5, \ 1, \ 3, \ 4.$$

Plasma jets have been studied numerically and experimentally by many authors. D. HUGHES and WOODING [34] numerically solved scattering problem for inhomogeneous plasma torch column with $n_e = n_{e0}(1 - r^2 / R^2)$ using RUNGE--KUTTA technique. FAUGERAS [7] used the method of selfconsisting field. He got the scattering field in integral form for the case of parallel polarization and made computation for different possible electron density profiles which are reasonable in plasma jets, with which he experimentally worked. G. GAL and W. GIBSON [31] have studied numerically e.m.w. interaction with jets having Gaussian electron density profile.

In this work we have treated the scattering by infinitely long, inhomogeneous across the radius, plasma column enclosed by the glass tube with arbitrary electron density distribution. Using power series method the relevant contour problem was solved for the case of parallel polarization covering the interval of parametar $R/\lambda$ from 0.1 to 10.0 numerically and from 0.27 to 2.92 experimentally using equipment in $X$ and $Q$ band. All these computations comprising very wide range of electron densities at axis from $0.001\,n_c$ to $100.0\,n_c$. For the case of normal polarization the sheet method was used.

Processes responsible for plasma decay have been separated and ambipolar diffusion and radiative recombination coefficients have been measured, using microwave scattering diagnostic technique, for all inert gases.

## 1. THEORY

### 1.1. Electromagnetic Equations for Scattering Problem

Scattering of electromagnetic radiation by an inhomogeneous infinitely long plasma column enclosed by the glass tube, in the case when the plasma radius and wavelength of incident radiation in free space are of the same order of magnitude, must be treated by the exact solution of corresponding MAXWELL equations for the given contour problem.

In MKSA unit system MAXWELL equations are

$$(1.1) \qquad \operatorname{rot} \vec{K} = -\frac{\partial \vec{B}}{\partial t},$$

$$(1.2) \qquad \operatorname{rot} \vec{H} = \vec{J} + \frac{\partial \vec{D}}{\partial t},$$

$$(1.3) \qquad \operatorname{div} \vec{D} = \rho,$$

$$(1.4) \qquad \operatorname{div} \vec{B} = 0,$$

where $\rho$ is free charge volume density and $\vec{J}$ is convection current density.

$$(1.5) \qquad \vec{D} = \varepsilon_0 \vec{K},$$

$$(1.6) \qquad \vec{H} = \frac{\vec{B}}{\mu_0},$$

$$(1.7) \qquad \vec{J} = \sigma \vec{K},$$

where $\varepsilon_0$ and $\mu_0$ are dielectric constant and permitivity of free space and $\sigma$ is specific electrical conductivity for a given medium.

We shall suppose that electric and magnetic fields have variation in time as

$$(1.8) \qquad\qquad \exp(i\,\omega\,t).$$

After some simple transformations it is easy to get the following differential equations for the electric and magnetic fields

$$(1.9) \qquad\qquad \nabla^2 \vec{K} + \omega^2\,\varepsilon\,\mu\,\vec{K} + \mathrm{grad}\,\left(\frac{\vec{K}\cdot\mathrm{grad}\,\varepsilon}{\varepsilon}\right) = 0,$$

$$(1.10) \qquad\qquad \nabla^2 \vec{H} + \omega^2\,\varepsilon\,\mu\,\vec{H} + \frac{\mathrm{grad}\,\varepsilon}{\varepsilon} \times \mathrm{rot}\,\vec{H} = 0,$$

where $\varepsilon$ is complex dielectric constant

$$(1.11) \qquad\qquad \varepsilon = \varepsilon_0 - i\,\frac{\sigma}{\omega},$$

and $\mu = \mu_0$ (See V. L. GINZBURG [8]). Equations (1.9) and (1.10) have not to be solved both but only one of them, and the other corresponding field could be obtained from MAXVELL rot Eqs.

Because of cylindrical symetry, z components of Eqs. (1.9) and (1.10) together with $r$ and $\theta$ components of MAXWELL rot Eqs. give us

$$(1.12) \qquad
\begin{aligned}
&\frac{1}{r}\frac{\partial}{\partial r}\left(r\,\frac{\partial K_z}{\partial r}\right) + \frac{1}{r^2}\frac{\partial^2 K_z}{\partial \theta^2} + \omega^2\,\varepsilon\,\mu\,K_z = 0,\\[8pt]
&H_r = -\frac{1}{i\,\mu\,\omega}\frac{\partial K_z}{\partial \theta}\frac{1}{r},\\[8pt]
&H_\theta = \frac{1}{i\,\mu\,\omega}\frac{\partial K_z}{\partial r},
\end{aligned}$$

$$(1.13) \qquad
\begin{aligned}
&\frac{1}{r}\frac{\partial}{\partial r}\left(r\,\frac{\partial H_z}{\partial r}\right) + \frac{1}{r^2}\frac{\partial^2 H_z}{\partial \theta^2} + \omega^2\,\mu\,\varepsilon\,H_z - \frac{1}{\varepsilon}\frac{d\varepsilon}{dr}\frac{\partial H_z}{\partial r} = 0,\\[8pt]
&K_r = \frac{1}{i\,\varepsilon\,\omega}\frac{\partial H_z}{\partial \theta}\frac{1}{r},\\[8pt]
&K_\theta = \frac{-1}{i\,\varepsilon\,\omega}\frac{\partial H_z}{\partial r}.
\end{aligned}$$

Knowing $H_z$ and $K_z$, components $H_r$, $H_\theta$, $K_r$ and $K_\theta$ could be obtained easely from the above systems of Eqs. (1.12) and (1.13). Therefore, two modes are of special interest:

1. TM mode, or the case of **parallel polarization, when** $\vec{K} = \vec{e}_z K_z$, and Eqs. (1.12) and (1.13) are becoming now

$$\frac{1}{r}\frac{\partial}{\partial r}\left(r\frac{\partial K_z}{\partial r}\right) + \frac{1}{r^2}\frac{\partial^2 K_z}{\partial \theta^2} + \omega^2\,\varepsilon\mu\,K_z = 0,$$

$$K_r = K_\theta = 0,$$

(1.14) $$\qquad H_r = \frac{-1}{i\mu\omega}\frac{\partial K_z}{\partial \theta}\frac{1}{r},$$

$$H_\theta = \frac{1}{i\mu\omega}\frac{\partial K_z}{\partial r},$$

$$H_z = 0.$$

2. TE mode, or the case of normal polarization when $\vec{H} = \vec{e}_z H_z$, with Eqs. (1.12) and (1.13) becoming then

$$\frac{1}{r}\frac{\partial}{\partial r}\left(r\frac{\partial H_z}{\partial r}\right) + \frac{1}{r^2}\frac{\partial^2 H_z}{\partial \theta^2} + \omega^2\,\mu\varepsilon\,H_z - \frac{1}{\varepsilon}\frac{d\varepsilon}{dr}\frac{\partial H_z}{dr} = 0,$$

$$H_\theta = H_r = 0,$$

(1.15) $$\qquad K_r = \frac{1}{i\varepsilon\omega}\frac{\partial H_z}{\partial \theta}\frac{1}{r},$$

$$K_\theta = -\frac{1}{i\varepsilon\omega}\frac{\partial H_z}{\partial r},$$

$$\varepsilon(r,\omega)K_z = 0.$$

The principal difference between Eqs. (1.14) and (1.15) is in the first and last Eqs. of the systems. The structure of Eqs. for TE mode is more complicated than for TM mode. For TM mode we have pure transfersal wave ($H_z = 0$), but for TE mode $K_z$ is equal zero only when $\varepsilon \neq 0$. However, it is easy to have a plasma column with $\varepsilon = 0$ at some radius $r = r_0$ and there could exist electron plasma waves (V. L. Ginzburg [8]).

### 1.2. Solution of Differential Equations for Components $K_z$ and $H_z$

Looking for the solutions of Eqs. (1.14) and (1.15) in the form

$$R(r)\,\Theta(\theta),$$

one gets the following equations

$$\frac{d^2\Theta}{d\theta^2} + n^2\,\Theta = 0,$$

(1.16)

$$\frac{d^2 R}{dr^2} + \frac{1}{r}\frac{dR}{dr} + \left(\omega^2\,\mu\varepsilon - \frac{n^2}{r^2}\right)R = 0,$$

for the case of parellel polarization, and

$$\frac{d^2\Theta}{d\theta^2} + n^2 \Theta = 0,$$

(1.17)

$$\frac{d^2R}{dr^2} + \left(\frac{1}{r} - \frac{1}{\varepsilon}\frac{d\varepsilon}{dr}\right)\frac{dR}{dr} + \left(\omega^2\mu\varepsilon - \frac{n^2}{r^2}\right)R = 0,$$

for the case of normal polarization.n is some number which has to be defined. As $\Theta(\theta)$ has to be unique it comes out

$$n = 0, \pm 1, \pm 2, \pm 3, \ldots$$

and solutions of the first equation from the systems (1.14) and (1.15) are

(1.18)
$$\sum_{n=-\infty}^{+\infty} R_n(r) \cos n\theta,$$

where $R_n(r)$ are solutions of differential equations (1.16) for $K_z$ and (1.17) for $H_z$ respectively.

## 1.3. Radial Equation Solution

1.3.1. *Homogeneous Plasma Column.* — Radial differential equations have the same form for TM and TE mode for homogeneous plasma column, becoming BESSEL differential equations

(1.19)
$$\frac{d^2R}{dr^2} + \frac{1}{r}\frac{dR}{dr} + \left(k^2 - \frac{n^2}{r^2}\right)R = 0,$$

where $k^2 = \omega^2\mu\varepsilon$ is square of complex wave number for a given medium. The solution for $R_n(r)$ is

(1.20)
$$R_n(r) = A_n J_n(kr),$$

where $A_n$ are integration constants and $J_n(kr)$ BESSEL functions of first kind and $n^{th}$ order. Second solution $Y_n(kr)$ has a singularity for $r = 0$ and is of no interest here.

1.3.2. *Inhomogeneous Plasma Column.* — Radial differential equation could be solved in this case exactly only for limited number of special cases. But, unfortunately, those cases have not considerable physical or practical interest. They are only interesting for computations checking. Therefore, we shall use two approximate methods for radial equation solution: a) Power series method; b) Sheet method.

1.3.2 a. *Power Series Method.*

1.3.2 aa. *Parallel Polarization.* — If electron density profile in plasma column has quite arbitrary shape, dielectric constant of column could be represented by a potential power serie (or in polynomial form in special case) as

(1.21)
$$\varepsilon(r) = \sum_{m=0}^{\infty} a_m r^m,$$

where $a_m$ are complex constants determined in a way that (1.21) represents the best fit to real dielectric constant profile.

Introducing new dimensionless variable $x = k_f r$ equation (1.16) becomes

(1.22)
$$x^2 \frac{d^2 R}{dx^2} + x \frac{dR}{dx} + \left( x^2 \varepsilon_1 (x) - n^2 \right) R = 0,$$

where

(1.23)
$$\varepsilon_1 (x) = \sum_{m=0}^{\infty} b_m x^m,$$

and $b_m$ are complex constants $\left( b_m = a_m / \varepsilon_0 k_f^m \right)$.

The solution in the form

(1.24)
$$R_n (x) = \sum_{j=0}^{\infty} a_j x^j,$$

does not exist (PIAGGIO [16]), but using FROBENIUS method, solution can be expressed in the following form

(1.25)
$$R_n (x) = x^s \sum_{j=0}^{\infty} a_j x^j, \qquad (a_0 \neq 0),$$

where $s$ is some number.

Substituting (1.25) in (1.22) one gets

(1.26)
$$\sum_{j=0}^{\infty} \left( (s+j)^2 - n^2 \right) x^{s+j} + \left( \sum_{m=0}^{\infty} b_m x^m \right) \sum_{j=0}^{\infty} a_j x^{s+j+2} = 0^*.$$

for all values of $x$, i.e.

$$\frac{a_2}{a_0} = \frac{-b_0}{(s+2)^2 - n^2},$$

$$\frac{a_3}{a_0} = \frac{-b_1}{(s+3)^2 - n^2},$$

$$\frac{a_4}{a_0} = -\frac{\frac{a_2}{a_0} b_0 + b_2}{(s+4)^2 - n^2},$$

$$\vdots$$

$$\frac{a_{2k}}{a_0} = -\frac{\frac{a_{2k-2}}{a_0} b_0 + \frac{a_{2k-3}}{a_0} b_1 + \cdots + \frac{a_2}{a_0} b_{2k-4} + b_{2k-2}}{(s+2k)^2 - n^2},$$

$$\frac{a_{2k+1}}{a_0} = -\frac{\frac{a_{2k-1}}{a_0} b_0 + \frac{a_{2k-2}}{a_0} b_1 + \cdots + \frac{a_2}{a_0} b_{2k-3} + b_{2k-1}}{(s+2k+1)^2 - n^2},$$

---

* Here and before we implicitly supposed that series $\sum_{j=0}^{\infty} a_j x^j$ and $\sum_{m=0}^{\infty} b_m x^m$ are convergent for $x \leq x_0$ and therefore could be multiplied term by term.

Solutions for $s = -n$ and $s = +n$ are not independent and so we choose $s = +n$. Electric field is then

$$(1.28) \qquad K_z = \sum_{n=-\infty}^{+\infty} \left( x^n \sum_{j=0}^{\infty} a_j\, x^j \right) \cos(n\,\theta),$$

and magnetic field components $H_r$ and $H_\theta$ are

$$(1.29) \qquad H_r = \frac{-1}{i\,\mu\,\omega}\, \frac{1}{r}\, \frac{\partial K_z}{\partial \theta}, \quad H_\theta = \frac{1}{i\,\omega\,\mu}\, \frac{\partial K_z}{\partial r}\,.$$

Recurrence relations for $a_j$ are summarized in Appendix I for binomial electron density profiles and for the profile $\varepsilon_1(x) = b_0 + b_2\, x^2 + b_4\, x^4$.

1.3.2 ab. *Normal Polarization.* — Radial equation (1.17) for $H_z$ is

$$(1.30) \qquad x^2\, \frac{d^2R}{dx^2} + x\left(1 - \frac{x}{\varepsilon_1(x)}\, \frac{d\varepsilon_1}{dx}\right) \frac{dR}{dx} + \left(x^2\, \varepsilon_1(x) - n^2\right) R = 0.$$

Looking for the solution in the form (1.25) we have got

$$(1.31) \quad \left( \sum_{m=0}^{\infty} b_m\, x^m \right) \left\{ \sum_{j=0}^{\infty} \left((s+j)^2 - n^2\right) a_j\, x^{j+s} + \left( \sum_{m=0}^{\infty} b_m\, x^m \right) \sum_{j=0}^{\infty} a_j\, x^{j+s+2} \right\}$$

$$- \left( \sum_{m=0}^{\infty} b_m\, m\, x^{m-1} \right) \sum_{j=0}^{\infty} a_j\,(s+j)\, x^{j+s+1} = 0,$$

and

$$s = \pm n, \quad (a_0 \neq 0),$$

$$\frac{a_1}{a_0} = \frac{b_1\, s}{1\,(2s+1)\, b_0},$$

$$\frac{a_2}{a_0} = \frac{\dfrac{a_1}{a_0}\left(n^2 - (s+1)\, s\right) b_1 + \left(2\, b_2\, s - b_0^2\right)}{2\,(2s+2)\, b_0},$$

$$\frac{a_3}{a_0} = \frac{\dfrac{a_2}{a_0}\left(n^2 - (s+2)(s+1)\right) b_1 + \dfrac{a_1}{a_0}\left\{\left(n^2 - (s+1)(s-1)\right) b_2 - b_0^2\right\} + 3\, b_3\, s - 2\, b_0\, b_1}{3\,(2s+3)\, b_0},$$

$$\frac{a_4}{a_0} = \frac{\dfrac{a_3}{a_0}\left(n^2 - (s+3)(s+2)\right) b_1 + \dfrac{a_2}{a_0}\left\{\left(n^2 - (s+2)\, s\right) b_2 - b_0^2\right\}}{4\,(2s+4)\, b_0}$$

$$+ \frac{\dfrac{a_1}{a_0}\left\{\left(n^2 - (s+1)(s-2)\right) b_3 - 2\, b_0\, b_1\right\} + \left(n^2 - s\,(s-4)\right) b_4 - \left(2\, b_0\, b_2 + b_1^2\right)}{4\,(2s+4)\, b_0},$$

$$\frac{a_{2k}}{a_0} = \frac{\frac{a_{2k-1}}{a_0}\left(n^2 - (s+2k-1)(s+2k-2)\right)b_1 + \frac{a_{2k-2}}{a_0}\left\{\left(n^2 - (s+2k-2)(s+2k-4)\right)b_2 - b_0^2\right\}}{2k(2s+2k)b_0}$$

$$+ \frac{\frac{a_{2k-3}}{a_0}\left\{\left(n^2 - (s+2k-3)(s+2k-6)\right)b_3 - 2b_0b_1\right\}}{2k(2s+2k)b_0}$$

$$+ \frac{\frac{a_{2k-4}}{a_0}\left\{\left(n^2 - (s+2k-4)(s+2k-8)\right)b_4 - \left(2b_0b_2 + b_1^2\right)\right\}}{2k(2s+2k)b_0}$$

$$+ \frac{\frac{a_{2k-5}}{a_0}\left\{\left(n^2 - (s+2k-5)(s+2k-10)\right)b_5 - (2b_0b_3 + 2b_1b_2)\right\}}{2k(2s+2k)b_0}$$

$$+ \frac{\frac{a_{2k-6}}{a_0}\left\{\left(n^2 - (s+2k-6)(s+2k-12)\right)b_6 - (2b_0b_4 + 2b_1b_3 + b_2^2)\right\}}{2k(2s+2k)b_0} + \cdots$$

$$+ \frac{\frac{a_1}{a_0}\left\{\left(n^2 - (s+1)(s-2k+2)\right)b_{2k-1} + (2b_0b_{2k-3} + 2b_1b_{2k-4} + 2b_2b_{2k-5} + \cdots + 2b_{k-1}b_{k-2})\right\}}{2k(2s+2k)b_0}$$

$$(1.32) \qquad - \frac{\left(2b_0b_{2k-2} + 2b_1b_{2k-3} + 2b_2b_{2k-4} + \cdots + b_{k-1}^2\right) - 2ksb_{2k}}{2k(2s+2k)b_0} ,$$

$$\frac{a_{2k+1}}{a_0} = \frac{\frac{a_{2k}}{a_0}\left(n^2 - (s+2k)(s+2k-1)\right)b_1 + \frac{a_{2k-1}}{a_0}\left\{\left(n^2 - (s+2k-1)(s+2k-3)\right)b_2 - b_0^2\right\}}{(2k+1)(2s+2k+1)b_0}$$

$$+ \frac{\frac{a_{2k-2}}{a_0}\left\{\left(n^2 - (s+2k-2)(s+2k-5)\right)b_3 - 2b_0b_1\right\}}{(2k+1)(2s+2k+1)b_0}$$

$$+ \frac{\frac{a_{2k-3}}{a_0}\left\{\left(n^2 - (s+2k-3)(s+2k-7)\right)b_4 - \left(2b_0b_2 + b_1^2\right)\right\}}{(2k+1)(2s+2k+1)b_0}$$

$$+ \frac{\frac{a_{2k-4}}{a_0}\left\{\left(n^2 - (s+2k-4)(s+2k-9)\right)b_5 - (2b_0b_3 + 2b_1b_2)\right\}}{(2k+1)(2s+2k+1)b_0} + \cdots$$

$$+ \frac{\frac{a_1}{a_0}\left\{\left(n^2 - (s+1)(s-2k+1)\right)b_{2k} + (2b_0b_{2k-2} + 2b_1b_{2k-3} + 2b_2b_{2k-4} + \cdots + b_{k-1}^2)\right\}}{(2k+1)(2s+2k+1)b_0}$$

$$+ \frac{\left\{s(2k+1)b_{2k+1} - (2b_0b_{2k-1} + 2b_1b_{2k-2} + 2b_2b_{2k-3} + \cdots + 2b_{k-1}b_k)\right\}}{(2k+1)(2s+2k+1)b_0} .$$

1.3.2 ac. *Convergency.* — For the case of parallel polarization, solutions of radial equation are convergent for all values $x$ for which $\varepsilon_1(x)$ represented by serie (1.23) is convergent. For the case of normal polarization solutions in serie form are convergent for all values of $x$ for which expressions

$$Q(x) = x^2 \varepsilon_1(x) - n^2 \quad \text{and} \quad P(x) = -1 + \frac{x\dfrac{d\varepsilon_1}{dx}}{\varepsilon_1(x)},$$

represented by two power series $Q(x) = \sum\limits_{k=0}^{\infty} q_k x^k$ and $P(x) = \sum\limits_{k=0}^{\infty} p_k x^k$ are convergent (PIAGGIO [16]). For the dielectric constant of binomial form $\varepsilon_1(x) = b_0 + bx$, $\gamma = 1$, 2, 3 and 4 we have got that solutions are convergent for all
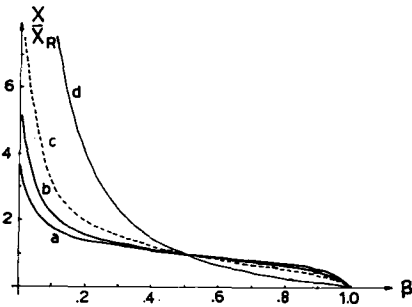


$a - \gamma = 1.$    $b - \gamma = 2.$    $c - \gamma = 3.$    $d - \gamma = 4.$

Fig. 1.1. Convergency curves for the solutions of Eq. (1.30) for different types of electron distributions for the case of normal polarization. Solutions of Eq. (1.30) converge into domain between the curve and coordinate axes for a loss-free plasma.
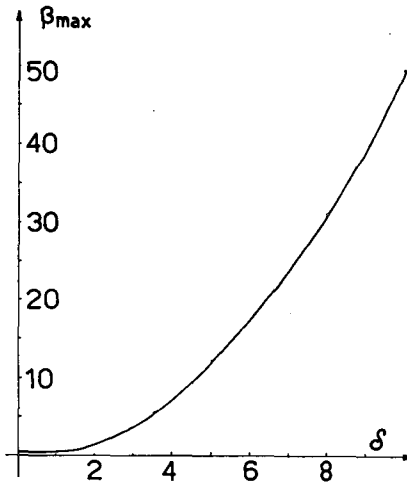


Fig. 1.2. Extreme values of parameteres $\beta_{max}$ and $\delta = \dfrac{\nu}{\omega}$ for which solutions of Eq. (1.30) are convergent in the region $x \leq x_R$ for the lossy plasma column with binomial electron distribution and for normal polarization.

values of $x$; in case of parallel polarization, and for $x \leq x_R \sqrt[2\gamma]{\dfrac{(\nu/\omega)^2 + (1-\beta)^2}{\beta^2}}$

in case of normal polarization, as is shown in Figs. 1.1 and 1.2.

Solutions of Eqs. (1.22) and (1.30) by the sheet method have been applied also as described in details by STANIĆ and WOODING [55].

## 1.4. Electromagnetic Field at the Receiver's Place

The diffraction field which is the sum of incident and scattering field could be expressed, using the radiation condition (J. STRATTON [20]), in the following form at receiver's place

$$(1.33) \qquad \sum_{n=0}^{\infty} \alpha_n \left\{ i^{-n} J_n (k_f \rho) + A_n H_n^{(2)} (k_f \rho) \right\} \cos (n\,\theta),$$

with $\alpha_n = \begin{cases} 1 \text{ for } n = 0 \\ 2 \text{ for } n = 1, 2, 3, \ldots \end{cases}$ , and $A_n$ are constants.

1.4.1. *Parallel Polarization.* — In this case constants $A_n$ are

$$(1.34) \qquad A_n = \frac{\det M_4^{pn}}{\det M_4^p},$$

where

$$(1.35) \quad M_4^p = \begin{Vmatrix} \Omega\,(R) & -J_n (k_g R) & -Y_n (k_g R) & 0 \\ \Omega_1\,(R) & -k_g J_n' (k_g R) & -k_g Y_n' (k_g R) & 0 \\ 0 & J_n (k_g R_g) & Y_n (k_g R_g) & -H_n^{(2)} (k_f R_g) \\ 0 & k_g J_n' (k_g R_g) & k_g Y_n' (k_g R_g) & -k_f H_n^{(2)'}(k_f R_g) \end{Vmatrix}$$

$\Omega$ and $\Omega_1$ are defined by Eq. (1.36) when the problem is treated by power series method and by corresponding expressions given in ref. [55] when the sheet method is used,

$$(1.36) \qquad \begin{aligned} \Omega\,(R) &= \sum_{j=0}^{\infty} \frac{a_j}{a_0} (k_f R)^{n+j} \ . \\ \Omega_1\,(R) &= k_f \cdot \frac{d\,\Omega}{d\,(k_f r)} \bigg|_{r=R} \ . \end{aligned}$$

Matrix $M_4^{pn}$ is different from the matrix $M_4^p$ only in the last column which has to have last two members $i^{-n} J_n (k_f R_g)$ and $k_f\, i^{-n} J_n' (k_f R_g)$ respectively.

Components of electromagnetic field are

$$(1.37) \qquad \begin{aligned} K_z\,(\rho) &= \sum_{n=0}^{\infty} \alpha_n \left( i^{-n} J_n (k_f \rho) + A_n H_n^{(2)} (k_f \rho) \right) \cos (n\,\theta), \\ H_\theta\,(\rho) &= \frac{1}{i\mu c} \sum_{n=0}^{\infty} \alpha_n \left( i^{-n} J_n' (k_f \rho) + A_n H_n^{(2)'}(k_f \rho) \right) \cos (n\,\theta), \\ H_r\,(\rho) &= \frac{1}{i\,\mu\,\omega\,\rho} \sum_{n=0}^{\infty} \alpha_n \left( i^{-n} J_n (k_f \rho) + A_n H_n^{(2)} (k_f \rho) \right) n \sin (n\,\theta). \end{aligned}$$

1.4.2. *Normal Polarization.* — In this case constants $A_n$ are

(1.38)
$$A_n = \frac{\det M_4^{nn}}{\det M_4^n} ,$$

where the matrix $M_4^n$ is

(1.39)
$$M_4^n = \begin{Vmatrix} \Omega(R) & -J_n(k_g R) & -Y_n(k_g R) & 0 \\ \Omega_2(R) & -k_g^{-1} J_n'(k_g R) & -k_g^{-1} Y_n'(k_g R) & 0 \\ 0 & J_n(k_g R_g) & Y_n(k_g R_g) & -H_n^{(2)}(k_f R_g) \\ 0 & k_g^{-1} J_n'(k_g R_g) & k_g^{-1} Y_n'(k_g R_g) & -k_f^{-1} H_n^{(2)'}(k_f R_g) \end{Vmatrix}$$

where $\Omega_2$ is defined by Eq. (1.40) and $\Omega$ by Eq. (1.36).

(1.40)
$$\Omega_2(R) = \frac{1}{k_f} \frac{d\Omega}{d(k_f r)} \bigg|_{r=R} .$$

The matrix $M_4^{nn}$ is different from the matrix $M_4^n$ only in the last column which has to have last two membars $i^{-n} J_n(k_f R_g)$ and $k_f^{-1} i^{-n} J_n'(k_f R_g)$ respectively.

Components of electromagnetic field are

(1.41)
$$H_z(\rho) = \sum_{n=0}^{\infty} \alpha_n \left( i^{-n} J_n(k_f \rho) + A_n H_n^{(2)}(k_f \rho) \right) \cos(n\theta),$$

$$K_\theta(\rho) = \frac{i}{\varepsilon_0 c} \sum_{n=0}^{\infty} \alpha_n \left( i^{-n} J_n'(k_f \rho) + A_n H_n^{(2)'}(k_f \rho) \right) \cos(n\theta),$$

$$K_r(\rho) = \frac{i}{\varepsilon_0 c \rho} \sum_{n=0}^{\infty} \alpha_n \left( i^{-n} J_n(k_f \rho) + A_n H_n^{(2)}(k_f \rho) \right) n \sin(n\theta).$$

## 1.5. Scattered Power and Phase at Receiver's Place

Scattered fields at receiver's place $r = \rho$ are

(1.42)
$$K_z^{\text{scatt}}(\rho) = \sum_{n=0}^{\infty} \alpha_n \left( A_n H_n^{(2)}(k_f \rho) \right) \cos(n\theta),$$

$$H_\theta^{\text{scatt}}(\rho) = -\frac{i}{\mu_0 c} \sum_{n=0}^{\infty} \alpha_n \left( A_n H_n^{(2)'}(k_f \rho) \right) \cos(n\theta),$$

for the case of parallel polarization, and

(1.43)
$$H_z^{\text{scatt}}(\rho) = \sum_{n=0}^{\infty} \alpha_n \left( A_n H_n^{(2)}(k_f \rho) \right) \cos(n\theta),$$

$$K_\theta^{\text{scatt}}(\rho) = \frac{i}{\varepsilon_0 c} \sum_{n=0}^{\infty} \alpha_n \left( A_n H_n^{(2)'}(k_f \rho) \right) \cos(n\theta),$$

for the case of normal polarization.

The mean value of POINTING vector for the scattering field (J. SURUTKA [21]) is then

(1.44)

$$\overline{\Gamma}_{||}^{\text{scatt}} = \frac{1}{2}\, \varepsilon_0 c \, \left| K_z^{\text{scatt}}(\rho) \right|^2,$$

$$\overline{\Gamma}_{\perp}^{\text{scatt}} = \frac{1}{2}\, \mu_0 c \, \left| H_z^{\text{scatt}}(\rho) \right|^2.$$

The phases of scattering fields $K_z^{\text{scatt}}$ and $H_z^{\text{scatt}}$ at the receiver's place are respectively

(1.45)

$$\Phi_{||} = \text{arctg}\, \frac{\text{Im}\left(K_z^{\text{scatt}}(\rho)\right)}{\text{Re}\left(K_z^{\text{scatt}}(\rho)\right)},$$

$$\Phi_{\perp} = \text{arctg}\, \frac{\text{Im}\left(H_z^{\text{scatt}}(\rho)\right)}{\text{Re}\left(H_z^{\text{scatt}}(\rho)\right)}.$$

## 2. EXPERIMENTAL SET-UP

### 2.1. Vacuum Equipment

Block diagram of vacuum system is shown in Fig. 2.1. Mechanical backing pump was connected in serie to oil diffusion pump. The best vacuum was $2 \cdot 10^{-7}$ Torr. Absolute measurement of pressure was done by two McLEOD gauges 0.001 — 1 Torr and 0.01 — 10 Torr. For relative pressure measurements BIR-VAC T101 PIRANI gauge (0.001—10 Toorr), BIR-VAC T1001 PENING gauge ($2.5 \cdot 10^{-2}$—$10^{-7}$ Torr) and radiofrequency LKB gauge (760——$10^{-3}$ Torr) have been used. Gas supply to the discharge tube was static or dynamic. Technically pure gases have been used for a dynamic vacuum and spectroscopically pure gases for static vacuum. To minimize gas penetration from the outside in the plastic pipe, the pressure in the pipe was higher than atmospheric pressure (I. A. MARDOCH [46]).
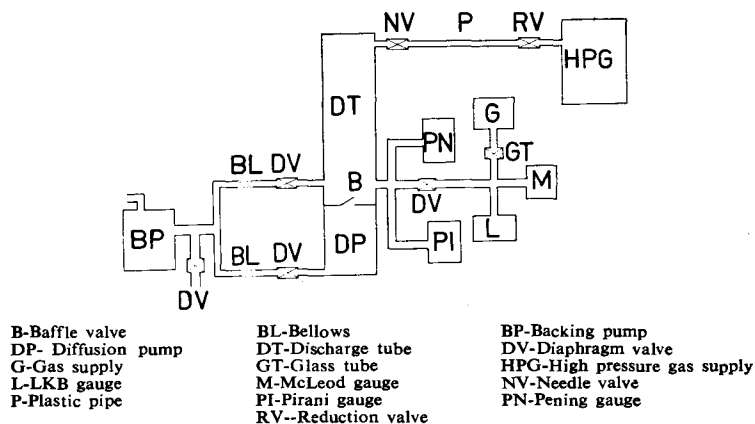


| B-Baffle valve | BL-Bellows | BP-Backing pump |
|---|---|---|
| DP- Diffusion pump | DT-Discharge tube | DV-Diaphragm valve |
| G-Gas supply | GT-Glass tube | HPG-High pressure gas supply |
| L-LKB gauge | M-McLeod gauge | NV-Needle valve |
| P-Plastic pipe | PI-Pirani gauge | PN-Pening gauge |
| | RV--Reduction valve | |

Fig. 2.1. Block diagram of vacuum system

## 2.2. Electrical Equipment

2.2.1. *Supply.* — Stationary gas discharge was obtained in argon at pressure range 0.3—1. Torr using a rectifier 2.5 kV/2 A and ceramic resistors 200—600 Ω. Breakdown was initiated by a TESLA coil. In a case of pulsed discharge, condenser with capacity 1 μ F charged to 5—10 kV was discharged through discharge tube and a spark gap. Typical discharge voltage was 6 kV. Time variation of discharge current is presented in Fig. 2.2.
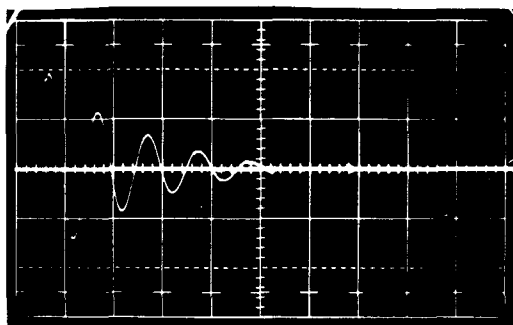


20 μ s/cm,       32 kA/cm         Probe resistance $R = 0.624$ m Ω.
Argon discharge at 0.3 Torr    Discharge radius $R_2 = 19.8$ mm.

Fig. 2.2. Discharge current variation in time

2.2.2. *Electrostatic Probes.* — Double electrostatic probes have been used for independent measurements of electron density and electron temperature in afterglow plasma. Probes were of tungsten wire 2 mm long and 0.25 mm in diameter. It was possible to move probes radially. Typical double probe current-voltage characteristic obtained in argon afterglow at 1 Toor, at 4 mm out of the axis of discharge, at $t = 250$ μ s after breakdown started, is shown in Fig. 2.3.

2.2.3. *Microwave Equipment.* — Reflex klystrons R 9555 EMI and 723 A/B Mullard have been used as a sources for microwave radiation in $Q$ and $X$ band respectively. Maximal relative variation of frequency was 0.03 % and power variation of 3 %. Block diagram of microwave set-up for measurement of angular variation of scattered power by stationary plasma column is shown in Fig. 2.4 a. Time variation of scattered power by afterglow plasma column at certain scattering angle $\theta$ is measured by microwave set-up shown in Fig. 2.4 b. Diodes IN 53 Sylvania and CV 21—54
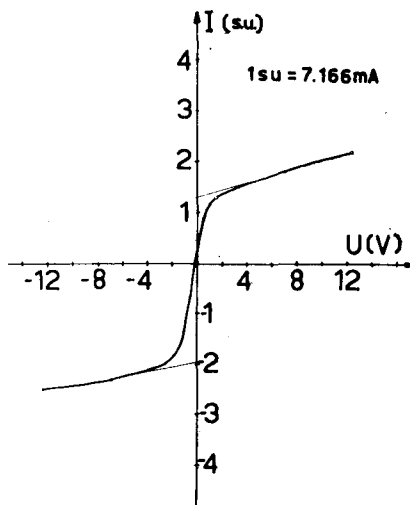


Fig. 2.3. Typical I-U double probe characteristic

Microwave Instruments Ltd. have been used for signal detection. All metal parts were covered by absorbers Echosorb as well as all room walls.
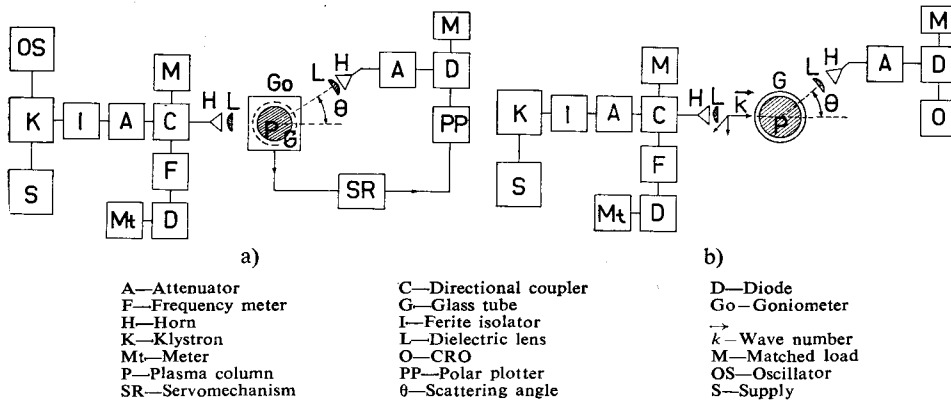


a)         b)

A—Attenuator    C—Directional coupler    D—Diode
F—Frequency meter    G—Glass tube    Go—Goniometer
H—Horn    I—Ferite isolator    $\vec{k}$—Wave number
K—Klystron    L—Dielectric lens    M—Matched load
Mt—Meter    O—CRO    OS—Oscillator
P—Plasma column    PP—Polar plotter    S—Supply
SR—Servomechanism    θ—Scattering angle

Eig. 2.4. Block diagram of microwave set-up

## 2.3. High Speed Photography Equipment

High speed photography technique has been used to prove theoretical supposition that plasma column is completely filling discharge tube. Beckman Whitley Inc. 501 image tube convertor camera was used with the exposition time 5, 10, 50, 100 and 1000 ns and built-in electronics for delays in the



AT—Autotransformer    IT—Isol. Transformer
HSC—High speed camera    TEK 162—Waveform generator
TEK 160—Stabilised voltage source    TI—Trigger pulse from discharge
TEK 163—Pulse generator    CRO 551—Tektronix CRO
CRO 543B—Tektronix CRO    M—Mains
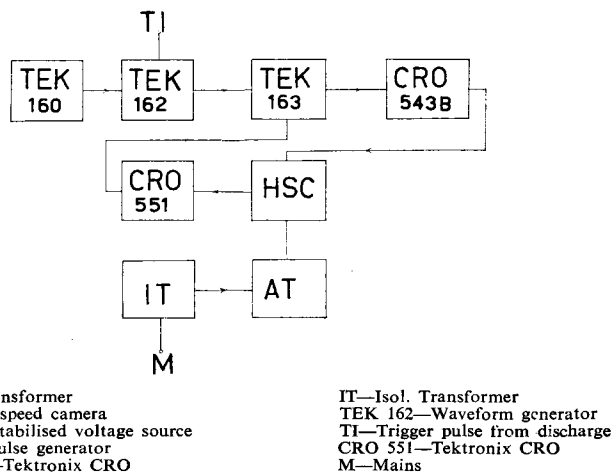
Fig. 2.5. Block diagram of electronic circuit for high speed camera triggering with delays greater than 100 μs.

range 0.5—100 μs. For delays greater than 100 μs the system shown in Fig. 2.5 was used. Camera had two objectives: first with the max. aperture $f_1/1.4$ focu-

sing the image to photocathode and second with the max. aperture $f_2/1.9$ for photographing the image from the anode. Polaroid film type 410 with the sensitivity 10000 ASA has been used. In Fig. 2.6 are shown the photographs of krypton discharge at different instants after breakdown was started. From the enclosed photos it is evident that the plasma column is filling entirely discharge tube in time interval 0-350 $\mu$ s for which the photos have been taken.
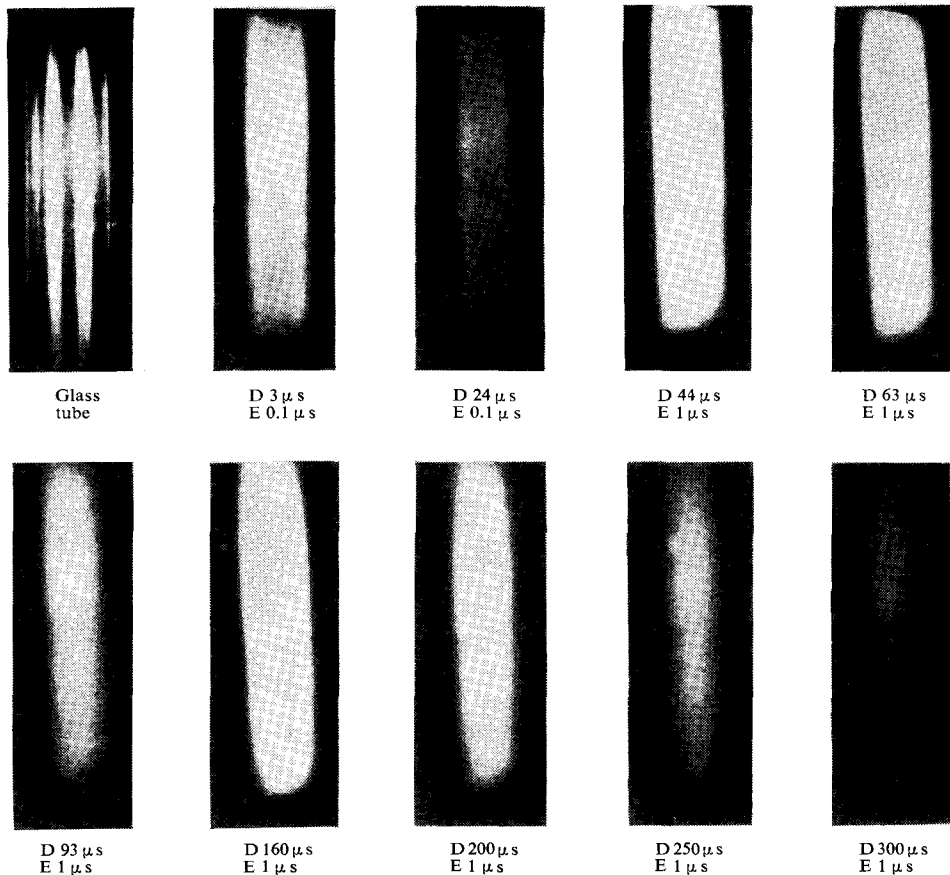


|       |       |       |       |       |
|-------|-------|-------|-------|-------|
| Glass tube | D 3 $\mu$ s  E 0.1 $\mu$ s | D 24 $\mu$ s  E 0.1 $\mu$ s | D 44 $\mu$ s  E 1 $\mu$ s | D 63 $\mu$ s  E 1 $\mu$ s |
| D 93 $\mu$ s  E 1 $\mu$ s | D 160 $\mu$ s  E 1 $\mu$ s | D 200 $\mu$ s  E 1 $\mu$ s | D 250 $\mu$ s  E 1 $\mu$ s | D 300 $\mu$ s  E 1 $\mu$ s |

Fig. 2.6. Photos of electrical gas discharge in krypton at 1 Torr at different stages after breakdown. For the first two photos of discharge, exposition was E 0.1 $\mu$ s and th? aperture $f_1/1.7$ and for all others E 1 $\mu$ s, $f_1/1.4$. Aperture of th? second objective was $f_2/5.6$ for delays D 3 $\mu$ s—D 93 $\mu$ s and $f_2/1.9$ for all others.

## 2.4. Mechanical Equipment

The goniometer with one fixed arm and one rotatable arm was used as a carrier of microwave equipment. (For details see A. R. JONES [12]). Position of goniometer was automatically controlled by servosystem and polar plotter. The picture of complete experimental arrangement is seen in Fig. 2.7.
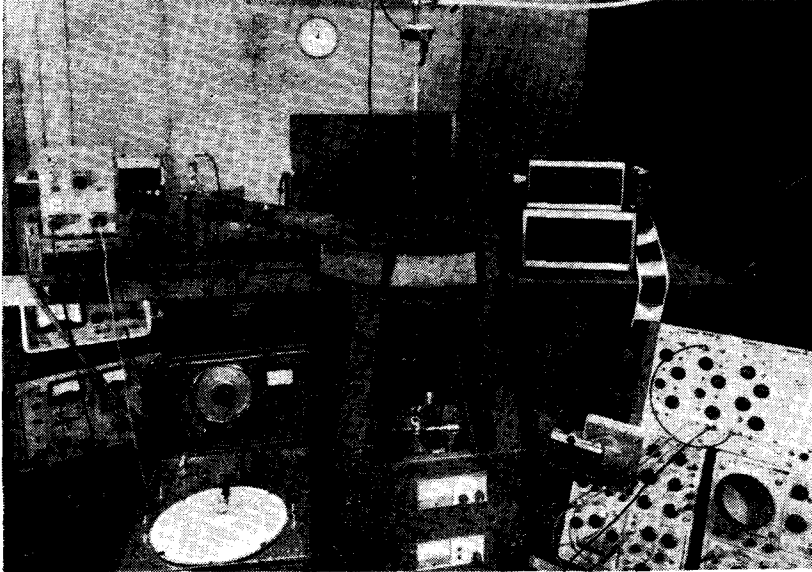
Fig. 2.7. Experimental Arrangement

## 3. EXPERIMENTAL AND NUMERICAL RESULTS

Microwave scattered power by cylindrical afterglow plasma column has been computed for four different column radii. Using microwave equipment in $X$ and $Q$ band the interval for $R/\lambda$ from 0.27 to 2.92 has been experimentally covered.

### 3.1. Afterglow Plasma Column

Experimental results for microwave scattered power on afterglow argon plasma column at 0.3 Toor are shown in Fig. 3.1. $Q$ band microwaves have been used. Column radius was $R_1 = 0.89$ cm. Corresponding numerical results are shown in the same figure varying $n_{e0}/n_c$ from 0. to 40.0. The scattered power at angle interval $0° < \theta < 40°$ has not been treated because of strong diffraction effects depending on the microwave beam shape, and therefore it was very difficult to compute diffraction field in that interval for $\theta \neq 0°$ because of very complex structure of real incident wave. In the angle interval $40° < \theta < 180°$ the electromagnetic field is a pure scattered field and therefore theoretical and experimental results have been compared there. The best agreement between computed and experimental results has been obtained for $\theta = 0°$. From the results in Fig. 3.1 it seems that the best fit profile of electron density is the profile of BESSEL type. There are also physical reasons to support this conclusion because at that range of pressures the main processes controlling plasma decay are processes of ambipolar diffusion. For other scattering angles there are great similarity between computed and experimental curves. It was noted that the extrema are more pronounced at computed than at experimental curves. One of the reasons for that is the finite size of the real receiver, receiving mean scattering signal from the angle interval $\theta_0 \pm \Delta\theta$ whereas the point type receiver was assumed in computation.

This could explain also relatively poor agreement for levels of scattered power by the glass tube without plasma because this power is at some angles very rapidly varying function with the change of angle.
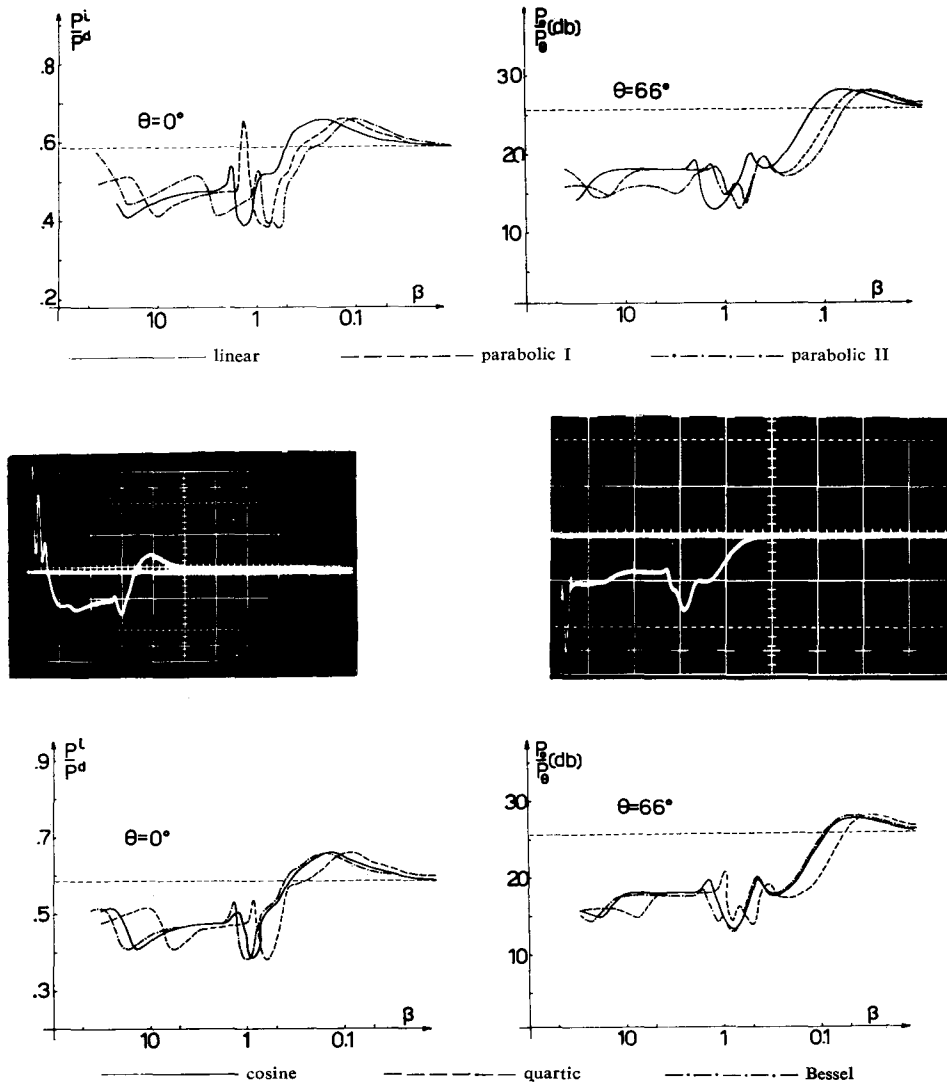


Fig. 3.1. Comparison of computed and experimental values of 35 GHz radiation scattered by a plasma column having various electron density distributions. The horizontal dashed lines represent the level of the power scattered by the glass tube $(R/\lambda = 1.04)$.

It is interesting to note that for the densities $n_{e0} < n_c$ practically all computed and experimental scattering curves have the same shape independent from the electron density profile. This could be explained by the glass tube masking effect on underdense plasma with considerably less dielectric constant at these

frequencies. Relative shifts of extrema at computed curves for different electron
density distributions in underdense region are caused by different mean values
of electron densities for different distributions.

In the overdense region $(n_{e0} > n_c)$ the shape of computed curves is
dependent on electron density distribution. From the Fig. 3.1 it is easy to
see that parabolic II profile $n_e = n_{e0}(1 - 0.7\, r^2/R^2)$ gives results considerably
different from all other computed and experimental results. This means that
the profile of this type is not probable.

Comparison between numerical and experimental results as a new diagnostic
technique has been suggested by JONES and WOODING [36]. The best results could
be obtained comparing extrema of computed and experimental scattering curves.
Corresponding extrema points of these two curves one gets that at $t = t_0$ electron
density, with known profile in afterglow plasma column, was at axis $n_{e0} = \beta\, n_c$,
where $\beta$ is read from the position of said extrema on computed curve. This
correspondence is possible because the time decay constant of plasma column
is considerably higher than period of incident radiaton. The main problem is
therefore to know electron density profile in plasma column. If the profile is
known from some independent measurements or by knowing the main processes
in plasma, then time variation of electron density at axis is obtained easely. In
many cases, however, the electron density profile is not known in advance and
one has to compute scattering curves for different reasonable electron profiles
and careful comparison with experimental results has to give a probable electron
density profile. The last technique is not convinient in many cases when electron
density profiles are variable in time. But in afterglow this was not the case.
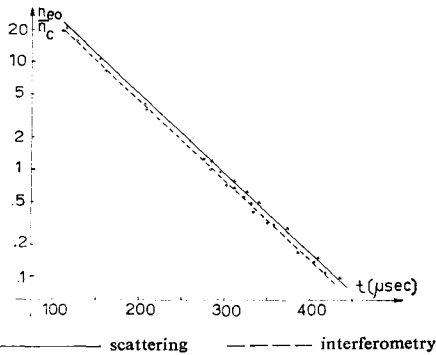


Fig. 3.2. Electron density time variation in
argon afterglow plasma at 0.3 Torr

Another inconvinience is the influence
of glass tube on scattered signal. This
could not be predicted in advance and
therefore for any new glass tube new
computations have to be done.

The time variation of electron den-
sity at axis in argon afterglow plasma
column at 0.3 Toor was obtained by the
above mentioned correspondence and
shown in Fig. 3.2. Values obtained from
different curves at various scattering angles
$\theta$ were scattered not more than 5%.
Interferometric measurements (see JONES,
STANIĆ and WOODING [38]) gave prac-
tically the same results.

The expermental curves of dif-
fracted power $P^d$ and scattered power $P_\theta$
have been shown together with corresponding computed curves in Fig. 3.3.
Electron profile was of BESSEL type and tube radius $R_2 = 1.2$ cm. Quite good
agreement has been obtainet at $\theta = 0°$, but at $\theta = 65°$ agreement was fair. Refferent
scattering levels from glass tube without plasma have been different and computed
extrema have had quite more pronounced shape than experimental ones.

Comparing these results with the results in Fig. 3.1 (tube with $R_1 = 0.89$ cm)
it is easy to see that here afterglow is starting later and decay process is longer.
The first result is consequence of the change of electric parameters of discharge
and the second one is the consequence of larger radius $(R_2 > R_1)$.

In Fig. 3.4 the experimental and computed scattering and diffraction curves have been presented for angles $\theta = 0°$, $60°$ and $110°$ for the glass tube with $R_3 = 1.98$ cm and in Fig. 3.5 the diffraction curves for $\theta = 0°$ and tube radius $R_4 = 2.5$ cm. It is characteristic for the two last families of curves (Fig. 3.4 and Fig. 3.5) that there is a flat part of about $400 \mu s$ (Fig. 3.4) and $630 \mu s$ (Fig. 3.5) and after that curves started to change. Numerical curves follow
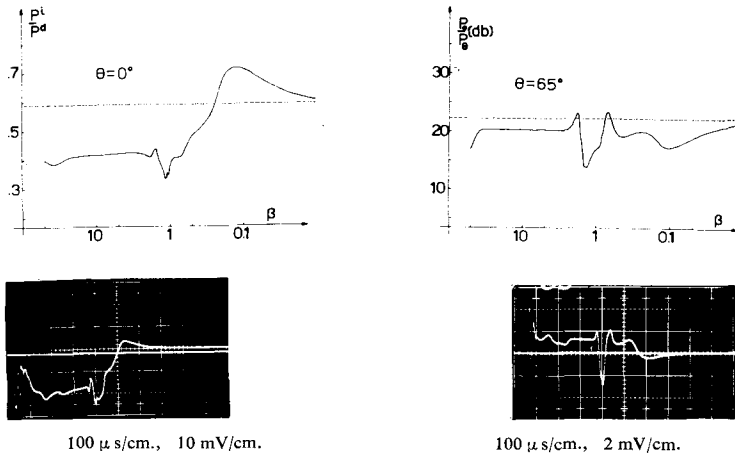


100 μs/cm.,  10 mV/cm.                   100 μs/cm.,  2 mV/cm.

Fig. 3.3. Comparison of computed and experimental values of 35 GHz radiation scattered by a plasma column having Bessel type electron density profile. ($R = 1.2$ cm).



200 μs/cm.,  20 mV/cm.          200 μs/cm.,  5 mV/cm.          200 μs/cm.,  2 mV/cm.
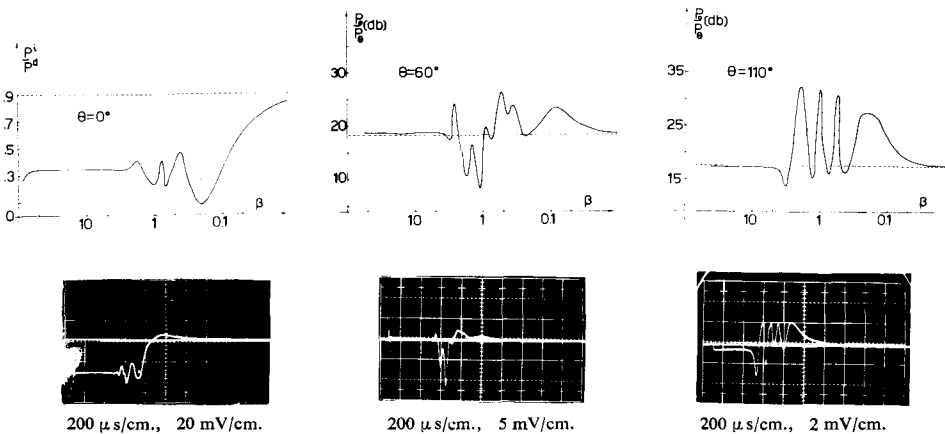
Fig. 3.4. Comparison of computed and experimental values of 35 GHz radiation scattered by a plasma column having Bessel type electron density distribution ($R = 1.98$ cm).

experimental ones. This could be explained noting that in both cases parameter $R/\lambda$ is 2.3 and 2.92 respectively and that in these cases we are very near to the region of geometrical optics approximation. Microwave beam at the early afterglow stages is incident on the strong overdense plasma column and could not see variation of electron densities inside plasma column unless electron

2*

density is approaching critical value. In the cases $R/\lambda \gg 1$ this transition is very sharp at $n_{e0} = n_c$ because in that case cylindrical geometry could be approximated by plane one and at $n_{e0} \approx n_c$ one has total reflection and microwave signal does not carry any information about changes inside the plasma column.
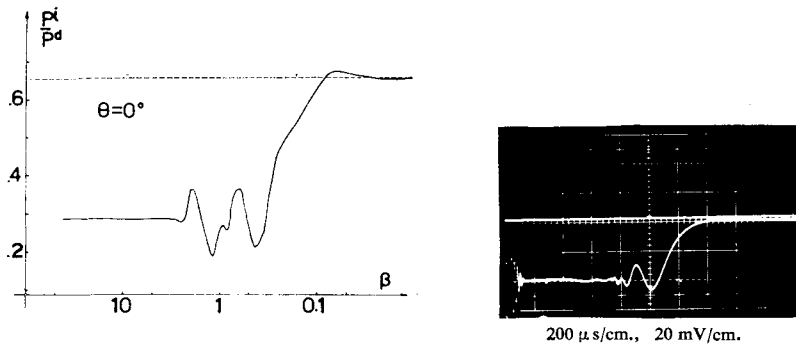


200 μs/cm.,  20 mV/cm.

Fig. 3.5. Comparison of computed and experimental values of 35 GHz radiation scattered by a plasma column having Bessel type electron density distribution ($R = 2.5$ cm).

Fig. 3.6 shows respectively experimental and computed curves for diffracted power on afterglow plasma columns in glass tubes with $R_1 = 0.89$ cm, $R_2 = 1.2$ cm and $R_4 = 2.5$ cm. All results reffer to $X$ band microwaves. A reasonable agreement between experimental and computed results is obtained.
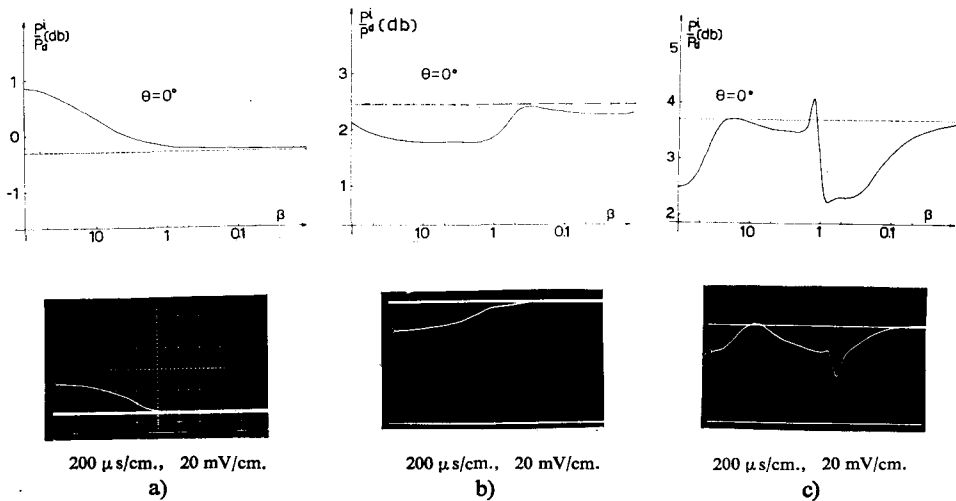


| 200 μs/cm.,  20 mV/cm. | 200 μs/cm.,  20 mV/cm. | 200 μs/cm.,  20 mV/cm. |
|:---:|:---:|:---:|
| a) | b) | c) |

Fig. 3.6. Comparison of computed and experimental values of 9.6 GHz radiation scattered by plasma column having Bessel type of electrom density distribution (a) $R = 0.89$ cm (b) $R = 1.2$ cm and (c) $R = 2.5$ cm

Therefore it could be concluded that, in the case of parallel polarization with the normal incidence, FROBENIUS power series method could be successfully applied in the transient region of parameter $R/\lambda$ not much greater than 1 and not much less than 1 and that agreement between theory and experiment is close.

The influence of the inhomogeneity of plasma column on the curves of diffracted ($\theta = 0°$) and scattered power ($\theta = 66°$) for the case of electron density profile of BESSEL type compared with homogeneous plasma has been shown in Fig. 3.7 a. Pronounced differences appear around critical density and in overdense region.



a)                                         b)

```
——————— homogeneous          ————— ν/ω=0.0  ·—·—·· ν/ω=0.5  —×—× ν/ω= 5.0
— — — — inhomogeneous         — — — ν/ω=0.1  —△—△ ν/ω=1.0  —▽—▽ ν/ω=10.0
```
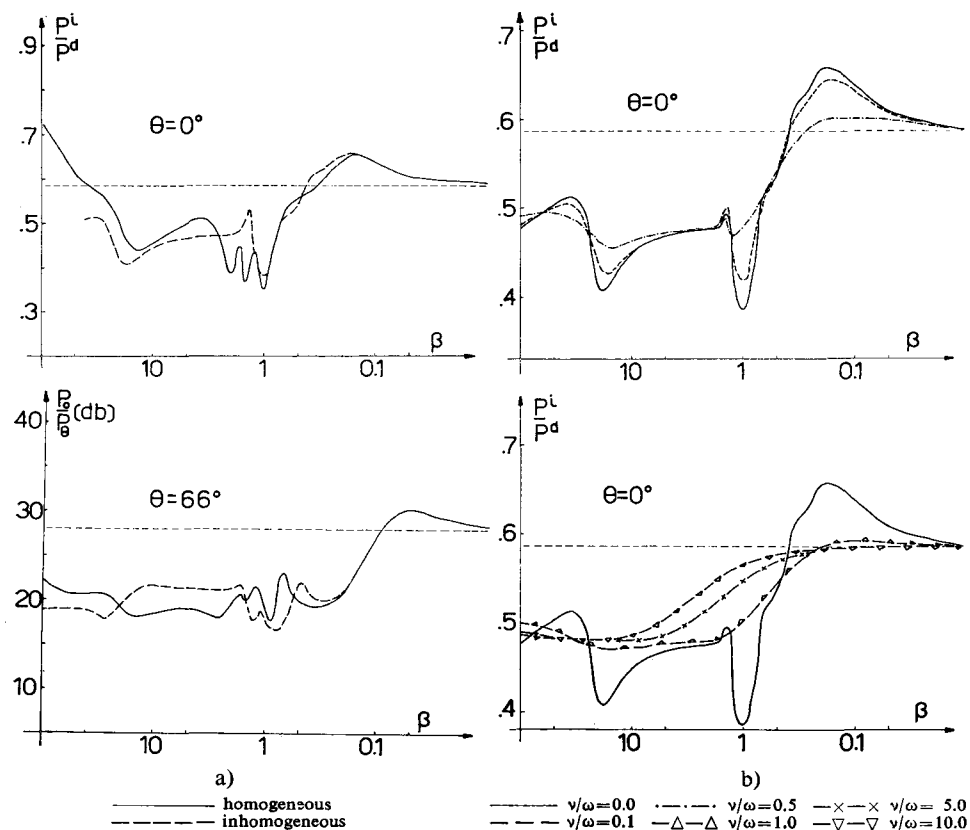
Fig. 3.7. Influence of inhomogeneity (a) and collision frequency (b) on the diffracted power curves for the case of parallel polarization $R/\lambda = 1.04$. $P^i$ — incident power of e. m. wave, $P^d$ — diffracted power at $\theta = 0°$, $P_\theta$ — scattered power at angle $\theta$.

The influence of collision frequency on the diffraction power curve is shown at computed curves in Fig. 3.7b. This influence is prominent when collision frequency for momentum transfer is the same order of magnitude as the frequency of incident waves. Comparing these numerical results with the corresponding experimental results for afterglow plasma in argon at $p = 0.3$ Toor it was found that collision frequency is much less than microwave frequency. (Independent measurements of collision frequency confirm these results).

### 3.2. Stationary Plasma Column

Using the apparatus shown in Fig. 2.4 a the angular variation of scattered power by stationary plasma column in argon, under the dynamic pressure in the range 0.3—1.0 Toor with maximum discharge current $I_a = 1.2\ A$, was obtained. Electron density in plasma column was considerably underdense when Q band microwave equipment was used and the influence of plasma column on scattered power is small as is seen from Fig. 3.8. In the angle range $0° \pm 30°$ there is some difference between scattering curves for glass tube with and without stationary plasma in it, but this range is not convinient for treatment as was explained earlier. In other angle ranges glass tube is practically masking the plasma column and the effects of plasma are negligible. To eliminate these masking effects it is necessary to increase electron density and acheave at least critical density of $1.53 \cdot 10^{13}\ el/cm^3$, and that is very difficult to acheave in ordinary stationary gas discharges. HUGHES and WOODING [34] therefore worked with the plasma torch at atmospheric pressure and with electron densities of $10^{15} — 10^{16}\ el/cm^3$. Another possibility is to work with capillary discharge column.
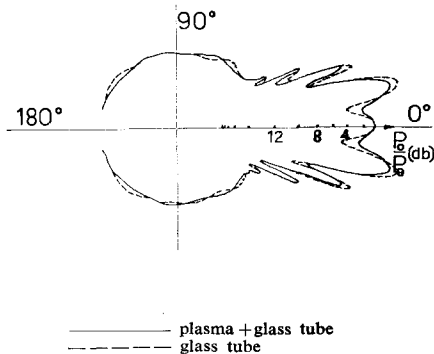


———— plasma + glass tube
— — — — glass tube

Fig. 3.8. Experimental angular variation of scattered power on D. C. argon plasma column ($I_a = 1$ A, $p = 1$ Torr, parallel polarization)
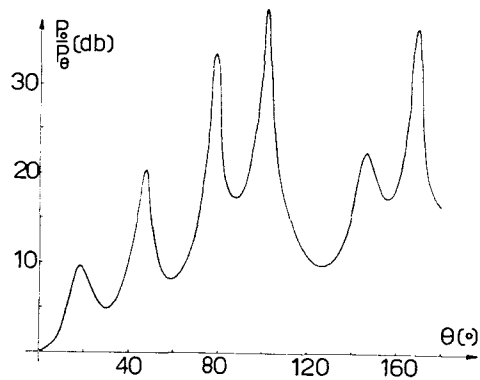
Fig. 3.9. Computed angular variation of scattered power by glass tube without plasma (parallel polarization)

3.2.1. *Influence of Electron Density Profile on Angular Variation of Scattered Power*. — For the stationary plasma column with the electron density profiles

(3.1)                $n_e = n_{e0}\,(1 - r^\gamma/R^r),\ \ \gamma = 0.5, 1, 2, 4\ \text{and}\ \infty,$

angular distribution of microwave scattered power in $X$ band has been computed using sheet method. Angular variation of scattered power by glass tube without plasma ($R_4 = 2.5$ cm) has been shown in Fig. 3.9. The curve has a rich structure with many geometrical resonances. When the plasma is introduced the position and the structure of resonances is changed as is seen from Fig. 3.10. For $\gamma = 0.5$ there is the difference in respect to homogeneous plasma ($\gamma = \infty$) because the resonances are more pronounced for homogeneous plasma. For $\gamma = 1$ there are the differences in angle interval $40° < \theta < 60°$ and $\theta > 120°$. For $\gamma = 2$ and $\gamma = 4$

the differences appear in the angle interval $20° < \theta < 130°$ where the resonances are slightly shifted and for $\theta > 130°$ the structure of curves is different.
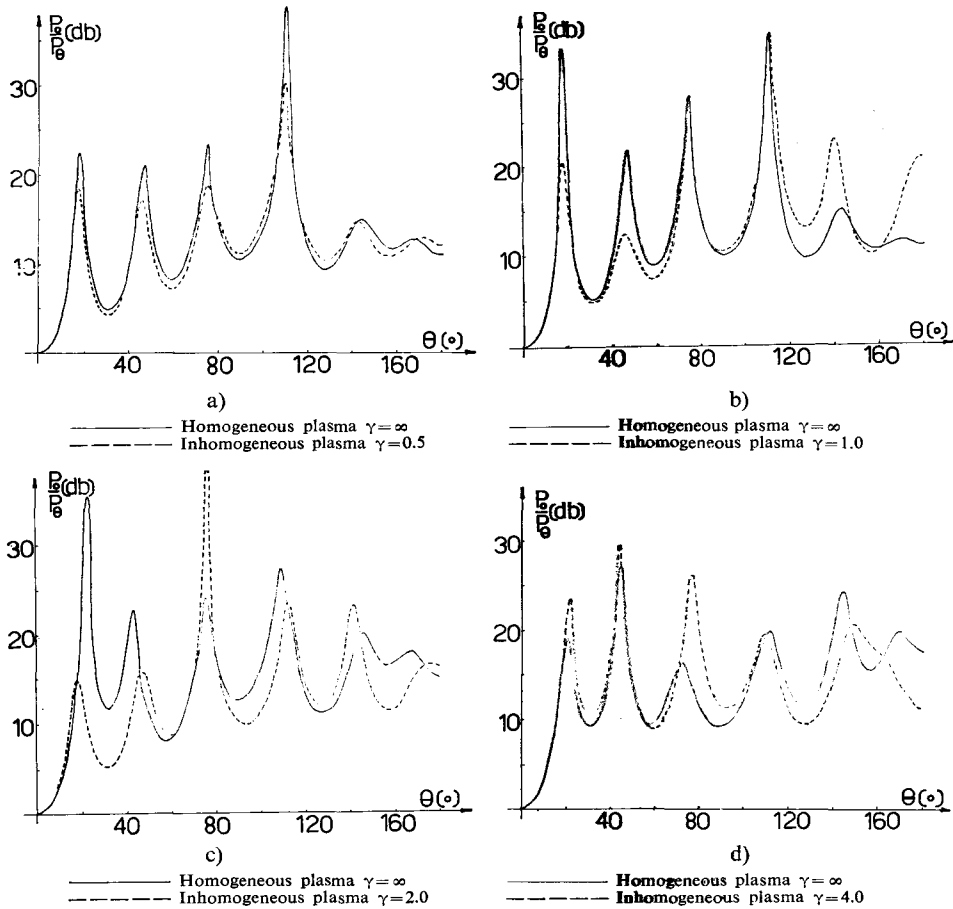


a)

———————— Homogeneous plasma $\gamma = \infty$
— — — — — Inhomogeneous plasma $\gamma = 0.5$

b)

———————— Homogeneous plasma $\gamma = \infty$
— — — — — Inhomogeneous plasma $\gamma = 1.0$

c)

———————— Homogeneous plasma $\gamma = \infty$
— — — — — Inhomogeneous plasma $\gamma = 2.0$

d)

———————— Homogeneous plasma $\gamma = \infty$
— — — — — Inhomogeneous plasma $\gamma = 4.0$

Fig. 3.10. Influence of inhomogeneity of D. C. plasma column on angular variation of scattered power for the case of parallel polarization ($n_{e_0}/n_e = 0.875$)

Numerical results have been checked directly by comparison with experimental results. So, it was possible to measure independently dielectric constant of glass tube at microwave frequencies. From the Fig. 3.11 it was evaluated that dielectric constant for pyrex glasss was between 4.4 and 4.5.



———————— $\varepsilon_g = 4.5$          — — — $\varepsilon_g = 4.4$
—·—·—· $\varepsilon_g = 4.3$          —o—o— experimental

Fig. 3.11. Comparison of numerical and experimental angular variations of scattered power on glass tube for different supposed values of dielectric constant for glass tube.
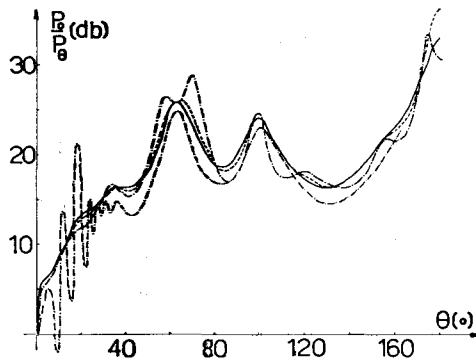
## 4. AMBIPOLAR DIFFUSION AND RECOMBINATION COEFFICIENTS
## MEASUREMENTS FOR INERT GASES BY MICROWAVE DIAGNOSTIC TECHNIQUE

### 4.1. General Consideration

In afterglow plasmas there are several mechanisms which more or less accelerate or decelerate decaying processes. In early stages of afterglow plasmas with monoatomic gases dominant processes are the processes of radiative recombination characterized by recmbination coefficient

$$(4.1) \qquad \alpha = \frac{1}{n_e^2} \frac{\partial n_e}{\partial t},$$

and multimode ambipolar diffusion.

In the later stages of afterglow, the processes of unimode ambipolar diffusion are dominant (diffusion with molecular and atomic ions). Ambipolar diffusion with molecular ions is possible in monoatomic gases by the conversion processes of atomic ion $Y^+$ in molecular ion $Y_2^+$

$$(4.2) \qquad Y^+ + 2\,Y \rightarrow Y_2^+ + Y,$$

by the collision of atomic ion with neutral. This process is characterized by the conversion rate $v_c$

$$(4.3) \qquad v_c = \beta_1 p_0^2,$$

where $p_0$ is pressure at Torr reduced to 0°C as a measure of gas density, and $\beta$ conversion coefficient.

Among the other porsible procecses, ionizing collisions of metastable atomic pairs have to be mentioned. In that case decay of atomic ions could be less than that expected only by the processes of ambipolar diffusion or recombination. We have neglected these processes because of low concentration of metastables in afterglow placma.

Impurities are alco important becaure they can drastically accelerate atomic ions rate decay by forming impurities ions by interection with atomic ions, or by electron attachment with molecular ions. We have used in all our experiments spectroscopically pure gases and therefore have neglected all these problems.

In the afterglow plasmas it is also very important to know electron, ion and neutral temperature. In the early stage of afterglow the electron temperature is higher than ion or neutral temperature but by collisions, mainly with neutrals, electron temperature is decaying. Radiation from metastables can decelerate the process of decaying electron temperature but the processes of ambipolar diffusion can has cooling effect so electron temperature can be lower than neutral temperature, as has been shown by BIONDI and CHANIN [27]. It is also known that on pulsed discharges (BORN [28]) with energy greater than 10 J neutral temperature is becoming higher than wall temperature of glass tube. In many papers, however, the thermodynamic equilibrium among plasma components i. e. $T_e \approx T_i \approx T_n = 300°\,K$ has been supposed, e. g. BIONDI and BROWN [26], SMITH and COPSEY [52], SMITH, GOODAL and COPSEY [54], SMITH and

CROMEY [53] and others. In all these papers the measurements of electron concentration, atomic ion concentration and molecular ion cocentration have been done in the very late stage of afterglow when the temperature equilibrium has ben achieved and when electron concentration is less than $5 \cdot 10^{10}$ el/cm$^3$. In our case using microwave scattering technique it was very difficult to measure very low electron concentration (much less than critical concentration) because in that case glass tube is masking the effect of plasma on the scattering signal, and so we have been restricted to study only the early stage of afterglow when $T_e > T_n$. Under the similar conditions NEWTON and SEXTON [47] worked with He.

### 4.2. Quantitative Analysis of Processes

For cylindrical plasma column of radius $R$ and the height $H = 2h$, time--space variation of atomic and molecular ion concentrations $n_1(r, t)$ and $n_2(r, t)$ for the weak ionized gas with no external magnetic field is defined by equations

$$(4.4) \qquad \frac{\partial n_1}{\partial t} = D_{a1} \nabla^2 n_1 - v_c n_1 - \alpha n_1^2,$$

$$(4.5) \qquad \frac{\partial n_2}{\partial t} = D_{a2} \nabla^2 n_2 + v_c n_1 - \alpha n_2^2,$$

where $D_{a1}$ and $D_{a2}$ are ambipolar diffusion coefficients with atomic and molecular ions respectively, $v_c$ is conversion rate of atomic in molecular ions and $\alpha$ s confficient of radiative recombination. Electron concentration is $n_e = n_1 + n_2$.

General solutions of Eqs. (4.4) and (4.5) are very complicated and we shall, therefore, treat three interesting cases which are relatively easy and have physical meaning and importance.

4.2.1. *Case when* $\alpha = 0$. — In the case when the processes of radiative recombination could be neglected Eqs. (4.4) and (4.5) were simplified. If we combine Eqs. (4.4) and (4.5) then it comes out

$$(4.6) \qquad \frac{\partial n_e}{\partial t} = D_a \nabla^2 n_e,$$

where $D_a = D_{a1} + D_{a2}$.

General solution of Eq. (4.6) is then

$$n_e(r, z, t) = \sum_{n,j} A_{nj} J_0\left( x_j \frac{r}{R} \right) \cos\left( \frac{2n-1}{2h} \pi z \right) \exp\left( -\frac{t}{\tau_{nj}} \right),$$

where $n = 1, 2, 3, \ldots$; $j = 1, 2, 3, \ldots$; $A_{nj}$ are integration constants,

$$(4.8) \qquad \frac{1}{D_a \tau_{nj}} = \left( \frac{1}{\Lambda_j} \right)^2 + \left( \frac{2n-1}{H} \pi \right)^2,$$

$\Lambda_j = R/x_j$, and $x_j = 2.405, 5.5, 11.891, \ldots$ are roots of BESSEL function $J_0(x)$ respectively.

For very long plasma columns $(h \to \infty)$ we have

(4.9)
$$\frac{1}{D_a \tau_j} = \frac{x_j^2}{R^2} = \frac{1}{\Lambda_j^2},$$

and electron density variation is then

(4.10)
$$n(r, t) = \sum_{j=1}^{\infty} A_j J_0 (r/\Lambda_j) \exp(-t/\tau_j),$$

where for each value $j = 1,2,3, \ldots$ we have corresponding mode of ambipolar diffusion with characteristic time constant $\tau_j$. Ratio between two values of these constants for $j = 1$ and $j = j$ is

(4.11)
$$\frac{\tau_1}{\tau_j} = \frac{x_j^2}{x_1^2},$$

and it is evident that higher modes vanish quickly i.e. $\tau_j \ll \tau_1$ for $j \gg 1$, and that very soon BESSEL type of electron density profile is formed and maintained in all afterglow period.

The existence of conversion processes is possible to detect by plotting $p_0/\tau_e$ against $p_0$, where $\tau_e$ is electron decay time constant. At higher pressures that curve has to be parallel with $p_0$ axis and it would define quantity $D_{a2} p_0$. At lower pressures that curve has to have the shape of cubic parabola determining the conversion coefficient $v_c$.

4.2.2. *Case when* $v_c \approx 0, n_2 \approx 0$. — In this case Eq. (4.4) is easy for solving if higher modes of diffusion have disappeared and if the electron density profile is not considerably changed in time. The constant $\tau_e = \tau_1$ is then

(4.12)
$$\frac{1}{\tau_1} = \frac{D_a}{\Lambda_1^2} + \beta_2 = -\frac{1}{n_e} \frac{\partial n_e}{\partial t},$$

where $1/\beta_2$ is time constant for electron concentration decay by volume processes, as for example recombination (i.e. $\beta_2 = \alpha n_e$). Multiplying Eq. (4.12) by $p_0$ we get

(4.13)
$$\frac{p_0}{\tau_1} = \frac{D_a p_0}{\Lambda_1^2} + \beta_2 p_0 = f(p_0).$$

If $f(p_0)$ is linear function of $p_0$ then it is possible to get parameters characterising ambipolar diffusion $(D)$ and radiative recombination $(\alpha)$, because the expression $p_0/\tau_1$ could be written down as

(4.14)
$$\frac{p_0}{\tau_1} = \left(\frac{p_0}{\tau_1}\right)_{p_0=0} + \beta_2 p_0,$$

where $(p_0/\tau_1)_{p_0=0} = (D_a p_0/\Lambda_1^2)_{p_0=0}$ determines $(D_a p_0)_{p_0=0}$ and slope determines radiative recombination coefficient $\alpha$ if the electron density is known.

This case is very close to our experimental conditions as it does not suppose thermodynamic equilibrium among plasma components and the product $D_a p$ is no more constant.
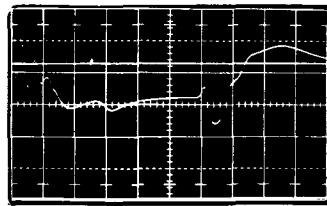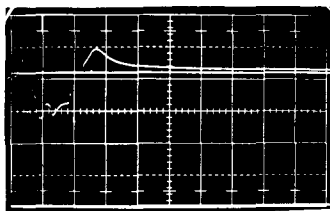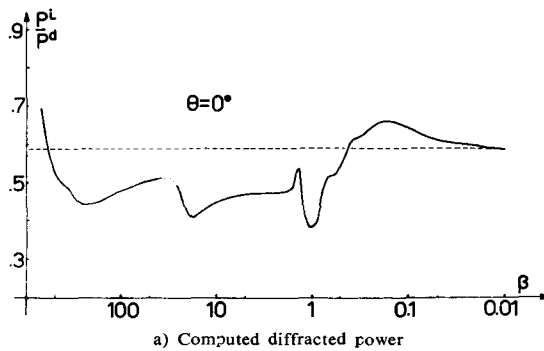
4.2.3. *Case when* $D_a \approx 0, v_c \approx 0$. — In the case when processes of radiative recombination are dominant from Eq. (4.4) we get
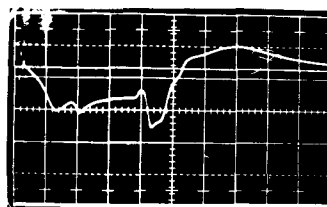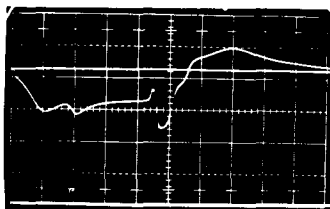
(4.15)
$$\frac{1}{n_e} = \frac{1}{n_e(0)} + \alpha\, t,$$

where $n_e(0)$ is electron density at $t = 0$. So, $1/n_e$ has to be linear function of time $t$.

## 4.3. Experimental and Numerical Results

All measurements in this chapter have been made for the tube with radius $R = 0.89$ cm. $(\Lambda_1^2 = 0.1369$ cm$^2)$. Q band $(\lambda = 8.55$ mm) microwaves have been used. Diffracted power $(\theta = 0°)$ and scattered power at $\theta = 66°$ and $96°$ were measured for different pressures in the tube. We have used practically all inert



a) Computed diffracted power



b) $p = 0.1$ Torr

c) $p = 0.35$ Torr

50 μs/cm., 20 mV/cm.

d) $p = 0.7$ Torr
100 μs/cm., 20 mV/cm.

e) $p = 2.2$ Torr
200 μs/cm., 20 mV/cm.

Fig. 4.1. Experimental curves for diffracted power by argon afterglow plasma column for different values of pressure in glass tube. All curves reffer to the case of parallel polarization

monoatomic gases and $N_2$. At each scattering angle $\theta$ we took three measurements and have treated only high reproducible results. Double electrostatic
probe technique for independent measurement of electron density and electron
temperature in plasma column (but only in argon plasma) has been also used.

Scattering power and diffraction power computation has been done under
the supposition that electron density profile in plasma column is of BESSEL
type, i.e. $J_0 (2.405\ r/R)n_{e0}$. This electron density profile is maintained in time
and so electron density decay is represented by decay of electron density at axis
of column $n_{e0}$. In fact, scattering power and diffraction power have been computed
for different values of parameters $n_{e0}/n_c$ from 0.0 to 700.0. Comparing experimental
and computed curves we have got parameter $n_{e0}/n_c$ and the instant of time
when electron density has that value. For afterglow plasma diagnostic we have
used the case of parallel polarization and for numerical solution of problem
power series method.

On Fig. 4.1 experimental curves of diffracted power have been shown for
argon afterglow at different pressures, and compared with computed curve for
diffraction power on collision free plasma column with BESSEL profile of electron
density. Experimental curves are practically useless for plasma diagnostic in very
early stage after breakdown because it is very difficult to eliminate interference
signals from the discharge. Decreasing time constant of external electric circuit,
this time interval could be reduced to a minimum, but the discharge is then
also changed. At lower pressures when the electron densities in afterglow plasma
are small, at experimental curves we can see only small part of complete
computed curve which corresponds to small densities (See Fig. 4.1 for $p = 0.1$
Toor). By increasing pressure we see more and more details of experimental
curves and it means that electron density is increasing. The upper limit for
pressure is defined by reproducibility of results in the first place. From the
computed curve on Fig. 4.1 it is seen that it is theoretically possible to follow the
variation of electron density over five decades (from $0.01\ n_{e0}/n_c$ to $\approx 700\ n_{e0}/n_c$).
In practical cases it is reduced to three or four decades for different scattering
angles at which numerical and experimental curves are compared.

4.3.1. *Ambipolar Diffusion Coefficient and Recombination Coefficient Measurements for Inert Gases.* — Variation of electron density in helium afterglow
plasma has been shown in Fig. 4.2 a. The electron density variation has been
followed in the range of three decades. The shape of curves is approximately
exponential. Decaying process is followed in time intervals from 50 $\mu s$ to 350 $\mu s$.
Supposing that ambipolar diffusion is dominant process for plasma decay it is
possible to determine ambipolar diffusion coefficient at various gas pressures
from the slope of curves in Fig. 4.2 a. These values for ambipolar diffusion
coefficients for different pressures are shown in Fig. 4.6.

If electron component in plasma column is in thermal equilibrium with
ions and neutrals then product $D_a p_0$ has to be constant. For helium at $T_e = 300°K$
(BIONDI and BROWN [26]) it was 556 cm$^2$ s$^{-1}$ Toor and that is considerably less
than maximum values we have got and which are in the range from 3100 to
8250 cm$^2$ s$^{-1}$ Toor. These differences are causad by thermal nonequilibrium i.e.
electron temperature until 350 $\mu s$ has not reached the value of ion or neutral
temperature in plasma column.

Taking into account the processes of radiative recombination, the values
for recombination coefficients could be obtained from the graphs of $p_0/\tau_e$ against

the pressure. The results of these measurements are shown in Fig. 4.2 b. Values for recombination coefficients are in the range $\alpha = 1.6 \cdot 10^{-8} - 1.6 \cdot 10^{-10}\,\text{cm}^3\,s^{-1}$ for the values of electron densities in the range $n_{e0} = 10^{14} - 10^{12}\,\text{el/cm}^3$ respectively.
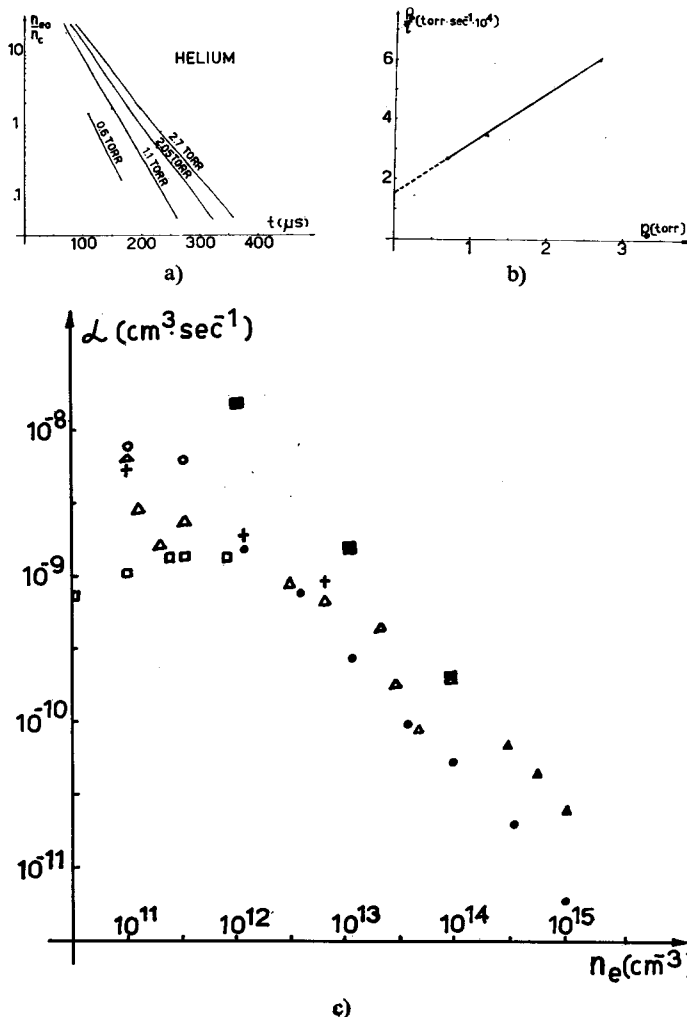


a)                                        b)



c)

⊠ — our results, ● — Newton, △ — Princeton, O — Aleksovski, □ — Mosburg, +— Anisimov, ▲ — Gusinov

Fig. 4.2. Experimental results for Helium

These values are in a reasonable agreement with the values of SEXTON and NEWTON [47], ALEXOWSKI and GRANOVSKI [22], MOSBURG, [45], GUSINOV and al. [32], ANISIMOV and al. [24] and with the results of PRINCETON group. Results for recombination coefficient obtained by other authors together with our results have been presented in Fig. 4.2 c in function of electron density. Our results are slightly higher. For $(D_a p_0)_{p_0=0}$ we have got the value $2160\,\text{cm}^2\,\text{s}^{-1}$ Toor. Conversion processes of atomic ions in molecular ions could be here neglected as the shape of curve $p_0/\tau_e$ is linear.

Electron density variation in neon afterglow plasma column is shown in Fig. 4.3 a. At lower pressures the high electron densities appear in very short time intervals (the earliest stages of afterglow) and then it is possible to follow electron density variation over approximately one decade. (See case of $p = 0.25$ Toor at Fig. 4.3 a). The product $D_a p$ is in the range of 800—2400 cm$^2$ s$^{-1}$ Toor and that is considerably higher than the value 110 cm$^2 \cdot$ s$^{-1}$. Toor at room temperature. The graph $p_0/\tau_e$ against $p_0$ has linear form as could be seen from Fig. 4.3 b. The recombination coefficient is in the range $\alpha = 5 \cdot 10^{-9} - 2 \cdot 10^{-10}$ cm$^3$ s$^{-1}$ for electron densities $n_{e0} = 10^{12} - 10^{14}$ el/cm$^3$. The value for $(D_a p_0)_{p_0=0} = 600$ cm$^2$ s$^{-1}$ Toor was obtained and it is also higher than the value at room temperature.



a) b)

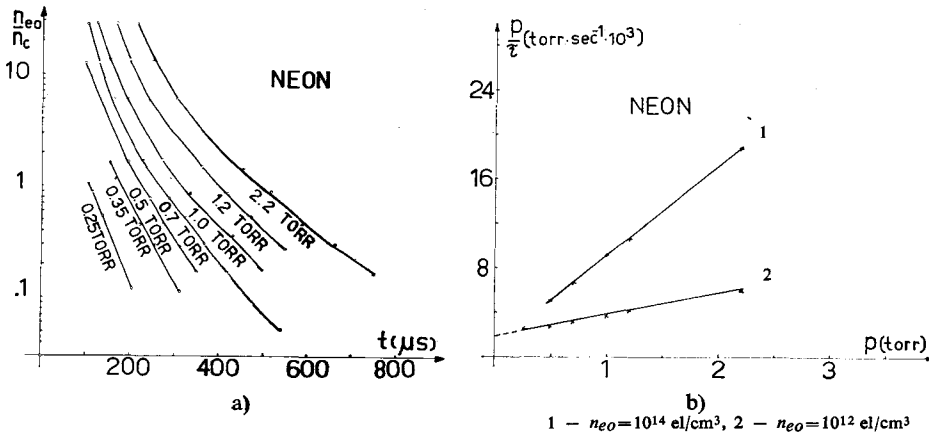1 — $n_{eo} = 10^{14}$ el/cm$^3$, 2 — $n_{eo} = 10^{12}$ el/cm$^3$

Fig. 4.3. Experimental results for Neon

In a similar way as in helium and neon it is possible from Fig. 4.4 a, where we have time variation of electron density in an argon plasma, to determine the maximum values of ambipolar diffusion coefficients $D_a$. At higher pressures the curves for $n_e(t)$ have not pure exponential character and therefore values for $D_a$ are determined in the later afterglow. These maximum values for $D_a$ are shown in Fig. 4.6 in function of pressure. Product of these values of $D_a$ and pressures $p$ is in the range from 780 to 1300 cm$^2$ s$^{-1}$ Toor and that is considerably higher than the corresponding value 150 cm$^2$ s$^{-1}$ Toor at 300° $K$ (KAYE and LABY [14]) Plotting $p_0/\tau_e$ against pressure for $p_0 > 1$ Toor, when it is reasonable to expect that recombination processes are considerable, it is possible to determine recombination coefficient and $(D_a p_0)_{p_0=0}$ from Fig. 4.4b. We have got for $\alpha = 6.65 \cdot 10^{-10} - 5.4 \cdot 10^{-8}$ cm$^3$ s$^{-1}$ for $n_{e0} = 10^{12} - 10^{14}$ el/cm$^3$ respectively and it agrees with the values of BROWN [4]. For $(D_a p_0)_{p_0=0}$ we obtained value 860 cm$^2$ s$^{-1}$ Toor. Using the data for mobilities $\mu^+$ of argon ions in argon (von ENGEL [6]) it is possible to evaluate electron temperature by relation

$$(4.16) \qquad T_e = \frac{e D_a}{k \mu^+},$$

where $k$ is BOLTZMANN constant. At pressure of 1 Toor we have got electron temperature $T_{e\,max} = 9950°K$ (for $D_a = 1030$ cm$^2$ s$^{-1}$ Toor). When the processes of

a)

b) $1 - n_{e0} = 10^{12} \text{ el/cm}^3$, $2 - n_{e0} = 10^{13} \text{ el/cm}^3$,
$3 - n_{e0} = 10^{14} \text{ el/cm}$

c)

d) $a - 150 \mu s$ $c - 250 \mu s$
$b - 200 \mu s$ $d - $ Bessel type of electron
distribution
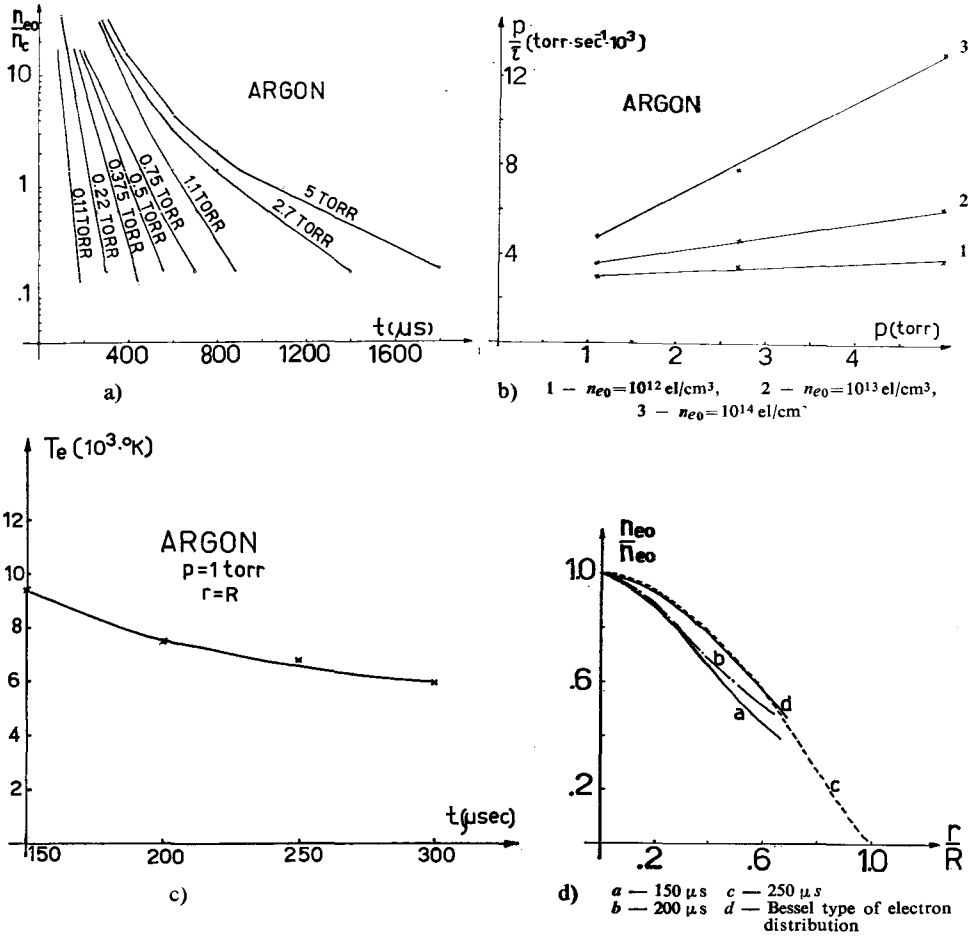
Fig. 4.4. Experimental results for Argon

a)

b) $1 - n_{e0} = 2 \cdot 10^{14} \text{ el/cm}^3$, $2 - n_{e0} = 5 \cdot 10^{12} \text{ el/cm}^3$
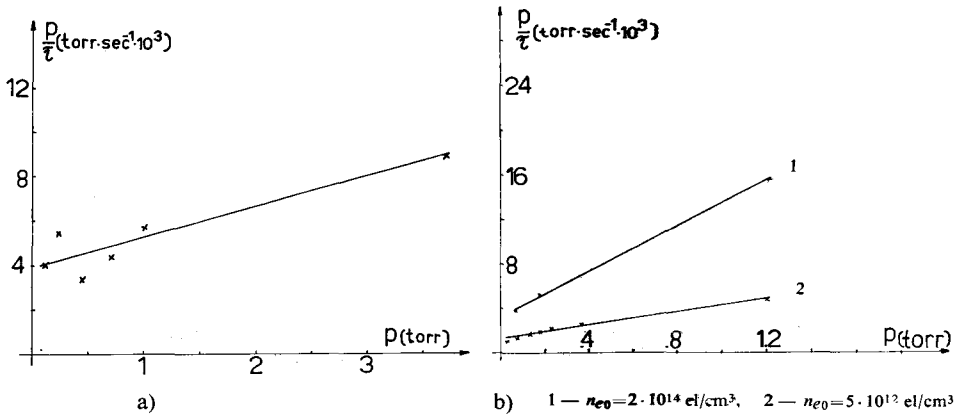
Fig. 4.5. Experimental results for (a) Krypton and (b) Xenon

radiative recombination are taken into account, the ambipolar diffusion coefficients become smaller and electron temperature is evalutated as 8200°K. These results for electron temperature are only indicative. Electron temperature dependence in argon plasma is obtained by double electrostatic probes at pressure of 1 Toor, and it is shown in Fig. 4.4 c. Electron density profile is measured in the early afterglow stage. It was shown that the electron density profile in argon afterglow at 1 Toor is not of BESSEL type in the early stage of afterglow, but later it becomes close to it. The possibilities for multimode ambipolar diffusion exist in early afterglow stage, but higher modes decay very fast as the eletron density profile approaches very fast the BESSEL type, and later on it is maintained. Time variation of electron density profiles is shown in Fig. 4.4 d.

For krypton, as is seen from Fig. 4.5 a, dependence of $p_0/\tau_e$ against pressure $p_0$ has not strictly linear character and it indicates that possibilities for processes of radiative recombination and some other processes are considerable. Rough linearization of this curve gives for radiative recombination coefficient values $10^{-8} - 10^{-10}$ cm$^3$ s$^{-1}$ for electron densities in the range $9 \cdot 10^{11} - -9 \cdot 10^{13}$ el/cm$^3$ and for $(D_a p_0)_{p_0=0} = 550$ cm$^2$ s$^{-1}$ Toor. However, it would be some type of equivalent picture of processes which can explain electron density decay, but the real processes by this technique cannot be obtained.

The product $D_a p$ for xenon is in the range $62-293$ cm$^2$ s$^{-1}$ Toor and this result is considerably higher than the value 10.5 cm$^2$ s$^{-1}$ Toor at room temperature. Dependence $p_0/\tau_e$ against $p_0$ for xenon is shown in Fig. 4.5 b. From these curves radiative recombination coefficient is obtained in the range $\alpha = 3 \cdot 10^{-10} - -2 \cdot 10^{-12}$ cm$^3$ s$^{-1}$ for electron densities in the range $n_{e0} = 5 \cdot 10^{12} - 2 \cdot 10^{-14}$ el/cm$^3$ The product $(D_a p_0)_{p_0=0}$ is 80 cm$^2$ s$^{-1}$ Toor.

The product $D_a p$ for nitrogen $N_2$ is in the range $880-1900$ cm$^2$ s$^{-1}$. Toor and it is considerably higher than at room temperature. Plotting dependence $p_0/\tau_e$ in function of pressure $p_0$ is not reasonable in this case because there are many possibilities for different processes. To separate them it is necessary to measure separately time variation of each sort of ions and electrons and that is impossible using this technique.
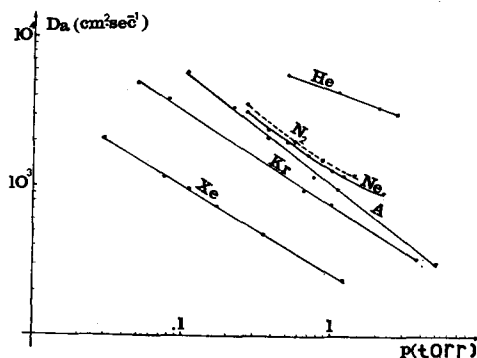


Fig. 4.6. Maximum values of ambipolar diffusion coefficients
for different gases in function of pressure

## 5. CONCLUSIONS

It was established that radial inhomogeneity has a considerable influence on angular variation of scattered power and therefore has to be taken into account.

Plasma column with an arbitrary electron density profile could be treated by the power series method in the case of parallel polarization but for normal polarization it is more convinient to use sheet method.

Numerically and experimentally are treated afterglow plasma columns enclosed by the glass tube. Parameter $R/\lambda$ was taken in the range 0.1 — 10.0 when it is impossible to use any of approximated methods for strongly overdense plasmas $(n_{e0} \gg n_c)$.

It was possible to follow electron density decay over four decades in the most favorable cases and over three decades in many other cases.

It was established that the most probable profile of electron density is $n_e = n_{e0} J_0 (2.405\, r/R)$ and it was confirmed by indenpendent double probe measurements.

Using microwave scattering by afterglow plasma column as a diagnostic tool the main processes responsible for plasma decay in early stages of afterglow are recognized.

In very early stages of afterglow very important processes are processes of radiative recombination. Radiative recombination coefficients for different inert gases have been measured and they are close to the existing results obtained by other more complicated methods.

Ambipolar diffusion coefficients have been measured in the early afterglow in a vide range of pressures from 0.01 to 6 Toor. Our results reffer to nonequilibrium plasma columns and therefore values for $D_a p$ are considerably higher than the existing results reffering to plasma in thermal equilibrium.

## APPENDIX I

Table of coefficients $\dfrac{a_j}{a_0}$ for Different Electron Density Distributions for the Case of Parallel Polarization

| Type of Distribution | $\dfrac{a_2}{a_0}$ | $\dfrac{a_3}{a_0}$ | $\dfrac{a_4}{a_0}$ | $\dfrac{a_{2k}}{a_0}$ | $\dfrac{a_{2k+1}}{a_0}$ | Interval of Convergency |
|---|---|---|---|---|---|---|
| Uniform $\varepsilon_1 = b_0$ | $\dfrac{-b_0}{2(2n+2)}$ | $0$ | $-\dfrac{b_0 \dfrac{a_2}{a_0}}{4(2n+4)}$ | $-\dfrac{b_0 \dfrac{a_{2k-2}}{a_0}}{2k(2n+2k)}$ | $0$ | |
| Linear $\varepsilon_1 = b_0 + b_1 x$ | „ | $-\dfrac{b_1}{3(2n+3)}$ | „ | $-\dfrac{b_0 \dfrac{a_{2k-2}}{a_0} + b_1 \dfrac{a_{2k-3}}{a_0}}{2k(2n+2k)}$ | $-\dfrac{b_0 \dfrac{a_{2k-1}}{a_0} + b_1 \dfrac{a_{2k-2}}{a_0}}{(2k+1)(2n+2k+1)}$ | |
| Quadratic $\varepsilon_1 = b_0 + b_2 x^2$ | „ | $0$ | $-\dfrac{b_0 \dfrac{a_2}{a_0} + b_2}{4(2n+4)}$ | $-\dfrac{b_0 \dfrac{a_{2k-2}}{a_0} + b_2 \dfrac{a_{2k-4}}{a_0}}{2k(2n+2k)}$ | $0$ | |
| Qubic $\varepsilon_1 = b_0 + b_3 x^3$ | „ | $-\dfrac{b_1}{3(2n+3)}$ | $-\dfrac{b_0 \dfrac{a_2}{a_0}}{4(2n+4)}$ | $-\dfrac{b_0 \dfrac{a_{2k-2}}{a_0} + b_3 \dfrac{a_{2k-5}}{a_0}}{2k(2n+2k)}$ | $-\dfrac{b_0 \dfrac{a_{2k-1}}{a_0} + b_3 \dfrac{a_{2k-4}}{a_0}}{(2k+1)(2n+2k+1)}$ | All values of $x$ |
| $\varepsilon_1 = b_0 + b_4 x^4$ | „ | $0$ | „ | $-\dfrac{b_0 \dfrac{a_{2k-2}}{a_0} + b_4 \dfrac{a_{2k-6}}{a_0}}{2k(2n+2k)}$ | $0$ | |
| $\varepsilon_1 = b_0 + b_2 x^2 + b_4 x^4$ | „ | $0$ | $-\dfrac{b_0 \dfrac{a_2}{a_0} + b_2}{4(2n+4)}$ | $-\dfrac{b_0 \dfrac{a_{2k-2}}{a_0} + b_2 \dfrac{a_{2k-4}}{a_0} + b_4 \dfrac{a_{2k-6}}{a_0}}{2k(2n+2k)}$ | $0$ | |

# REFERENCES

## Monographs and Ph. D. Thesis

1. M. ABRAMOWITZ and I. STEGUN: *Handbook of Mathematical Functions with Formulas, Graphs and Mathematical Tables*. National Bureau of Standards, Appl. math. series. 55, 1964.

2. Л. М. БРЕХОВСКИХ: *Волны в слоистых средах*. Изд. Акад. Наук СССР, Москва, 1957.

3. British Association for the Advancement of Sciences: *Mathematical Tables*, vols. 6 and 10. Cambridge, 1950.

4. S. C. BROWN: *Basic Data of Plasma Physics*. MIT Press, 1965.

5. R. M. CLEMENTS: *Experimental Investigation of Langmuir Probes*. Thesis for the degree of Ph. D. at the University of Saskatchewan, 1967.

6. A. von Engel: *Ionized Gases*. Oxford, 1965.

7. P. A. FAUGERAS: *Diffusion coherente d'une onde electromagnetique par un cylindre de plasma inhomogene*. Thesis pour le grade de docteur es-sciences a la centre d'Orsay, 1967.

8. В. Л. ГИНЗБУРГ: *Распространение электромагнитных волн в плазме*. Москва, 1967.

9. M. A. HEALD and C. B. WHARTON: *Plasma Diagnostic with Microwaves*. New York, 1965.

10. R. H. HUDDLESTONE and S. L. LEONARD: *Plasma Diagnostic Techniques*. New York, 1965.

11. H. C. van der Hulst: *Light Scattering by Small Particles*. London, 1957.

12. A. R. JONES: *Interaction of Electromagnetic Radiation with a Plasma Column*. Thesis for the degree of Ph. D. at the University of Wales, 1965.

13. Э. КАМКЕ: *Справочник по обыкновеним дифференцияльным уравнениям*. Москва, 1965.

14. G. W. C. KAYE and T. H. LABY: *Tables of Physical and Chemical Constants*. London, 1956.

15. D. S. MITRINOVIĆ i D. ĐOKOVIĆ: *Specijalne funkcije*. Beograd, 1964.

16. H. T. H. PIAGGIO: *An Elementary Treatise on Differential Equations*. London, 1944.

17. C. RICHARD: *Focussed Microwave Systems for Plasma Investigations*. Thesis for the degree of Ph. D. at the University of London, 1968.

18. L. G. SLATER: *Confluent Hipergeometric Functions*. New York, 1960.

19. В. И. СМИРНОВ: *Курс высшей Математики*, том II i III. Москва, 1958.

20. J. A. STRATTON: *Electromagnetic Theory*. New York, 1941.

21. J. SURUTKA: *Elektromagnetika*. Beograd, 1965.

## Papers

22. Y. M. ALEKSOVSKI and V. L. GRANOVSKI: Soviet Phys. — JETP **16**, (1963), 887.

23. B. ANIČIN: Radio Science, **69 D**, (1965), 721.

24. A. E. ANISIMOV and others: Sov. Phys. Tech. Phys. **7**, (1963), 884.

25. J. R. BARTHEL: Proc. of the I R E **50**, (1962), 10.

26. M. A. BIONDI and S. C. BROWN: Phys. Rev. **75**, (1949), 1700.

27. M. A. BIONDI and L. M. CHANIN: Phys. Rev. **94**, (1954), 910.

28. G. K. BORN and R. G. BUSER: J. Appl. Phys. **37**, (1966), 4918.

29. N. R. CITRON and J. DAVIS: Canadian J. of Phys. **44**, (1966), 2941.

30. L. A. Duškin and others: Soviet Physics — Technical Physics, **11**, (1967), 1372.
31. G. Gal and W. Gibson: IEEE Trans. on Ant. and Prop. AP-16, (1967), 468.
32. M. A. Gusinov and others: Phys. Rev. **149**, (1966), 91.
33. M. A. Heald: Culham Lab. Report CLM — R 34, (1964).
34. D. Hughes and E. R. Wooding: *Scattering of Microwaves by a Plasma Column*, Physics Department, University College of Wales, PPG 11, 1966.
35. W. von Ignatowsky: Ann. der Phys., **36**, (1905), 365.
36. A. R. Jones and E. R. Wooding: J. Appl. Phys., **37**, (1966), 4670.
37. A. R. Jones and E. R. Wooding: Electronics Letters, **1**, (1965), 171.
38. A. R. Jones, B. V. Stanić and E. R. Wooding: Electronics Letters, **4**, (1968), 392.
39. A. R. Jones and E. R. Wooding: University College of Wales, PPG **5**, 1964.
40. M. M. Z. Kharadly: Proc. IEE 110, (1963), 202.
41. M. Kerker and E. Matijević: Journal of Opt. Soc. of America, **51**, (1961), 506.
42. W. Lünov and M. Tutter: Plasma Physics, **9**, (1967), 97.
43. Y. Midzuno: J. Phys. Soc. Japan 16, (1961), 951.
44. Y. Midzuno: J. Phys. Soc. Japan 16, (1961), 1403.
45. E. R. Mosburg: Phys. Rev. **152**, (1966), 166.
46. I. A. Murdoch: Standard Telecomunication Lab. LABP 15—72.
47. A. A. Newton and M. C. Sexton: J. Phys. B. Ser. 2, **1**, (1968), 638.
48. J. V. Parker: Phys. Fluids 6, (1963), 1657.
49. P. M. Platzmam and H. T. Ozaki: J. Appl. Phys. 31, (1960), 1597.
50. Rayleigh: Phyl. Mag. **12**, (1881), 81.
51. J. Shmoys: J. Appl. Phys. 33, (1961), 689.
52. D. Smith and M. J. Copsey: J. Phys. B, Ser. 2, **1**, (1960), 650.
53. D. Smith and P. R. Cromey: J. Phys. B, Ser. 2, **1**, (1968), 638.
54. D. Smith, C. Goodal and M. Copsey: J. Phys. B, Ser. 2, **1**, (1968), 660.
55. B. Stanić and E. R. Wooding: Papers at 8th Inter. Conf. on Phenomena in Ionized Gases, Vienna, 1967, p. 522.
56. R. A. Stern: J. Appl. Phys 34, (1963), 2562.
57. D. J. H. Wort: Culham Lab. Report CLM-R 27, (1963).